



HAL
open science

A mathematical model to investigate the key drivers of the biogeography of the colon microbiota.

Simon Labarthe, Bastien Polizzi, Thuy Phan, Thierry Goudon, Magali Ribot, Béatrice Laroche

► **To cite this version:**

Simon Labarthe, Bastien Polizzi, Thuy Phan, Thierry Goudon, Magali Ribot, et al.. A mathematical model to investigate the key drivers of the biogeography of the colon microbiota.. 2018. hal-01761191v2

HAL Id: hal-01761191

<https://hal.science/hal-01761191v2>

Preprint submitted on 9 Oct 2018 (v2), last revised 6 Dec 2018 (v3)

HAL is a multi-disciplinary open access archive for the deposit and dissemination of scientific research documents, whether they are published or not. The documents may come from teaching and research institutions in France or abroad, or from public or private research centers.

L'archive ouverte pluridisciplinaire **HAL**, est destinée au dépôt et à la diffusion de documents scientifiques de niveau recherche, publiés ou non, émanant des établissements d'enseignement et de recherche français ou étrangers, des laboratoires publics ou privés.

A mathematical model to investigate the key drivers of the biogeography of the colon microbiota.

Simon Labarthe ^{1,*}, Bastien Polizzi ², Thuy Phan ³, Thierry Goudon ⁴, Magali Ribot ³, Beatrice Laroche ¹,

1 MaIAGE, INRA, Paris-Saclay University, Jouy-en-Josas, France,

2 IMFT, CNRS-INPT-Paul Sabatier University, Toulouse, FRANCE,

3 IDP, Université d'Orléans-CNRS, Orleans, FRANCE,

4 Université Côte d'Azur, Inria, CNRS, LJAD, Nice, FRANCE.

* Current Address: MaIAGE, INRA, Université Paris-Saclay, 78350 Jouy-en-Josas, France, Jouy-en-Josas
simon.labarthe@inra.fr

Abstract

The gut microbiota, mainly located in the colon, is engaged in a complex dialogue with the large intestinal epithelium through which important regulatory processes for the health and well-being of the host take place. Imbalances of the microbial populations, called dysbiosis, are related to several pathological status, emphasizing the importance of understanding the gut bacterial ecology. Among the ecological drivers of the microbiota, the spatial structure of the colon is of special interest: spatio-temporal mechanisms can lead to the constitution of spatial interactions among the bacterial populations and of environmental niches that impact the overall colonization of the colon. In the present study, we introduce a mathematical model of the colon microbiota in its fluid environment, based on the explicit coupling of a population dynamics model of microbial populations involved in fibre degradation with a fluid dynamics model of the luminal content. This modelling framework is used to study the main drivers of the spatial structure of the microbiota, specially focusing on the dietary fibres, the epithelial motility, the microbial active swimming and viscosity gradients in the digestive track. We found 1) that the viscosity gradients allow the creation of favourable niches in the vicinity of the mucus layer; 2) that very low microbial active swimming in the radial direction is enough to promote bacterial growth, which shed a new light on microbial motility in the colon and 3) that dietary fibres are the main driver of the spatial structure of the microbiota in the distal bowel whereas epithelial motility is preponderant for the colonization of the proximal colon; in the transverse colon, fibre levels and chemotaxis have the strongest impact on the distribution of the microbial communities.

1 Introduction

Humans host in their colon a large community of symbiotic microorganisms, the gut microbiota. Complex ecological cross-talks between the microbial populations and the gut epithelium are involved in the regulation of this community,

but also in the host homeostasis [32]. Microbial population imbalances, called dysbiosis, are now associated with number of physiopathological status, such as metabolic, auto-immune, inflammatory or even mental diseases[29, 30]. The microbial ecology of the gut is thus intensively studied in order to better understand the link between the gut microbiota and the host health and wellness by deciphering the mechanisms that shape the microbiota community structure.

Among them, the spatial organization of the microbiota plays an important role, both in the installation and maintenance of the microbiota, and impacts the host health, as recently outlined in [11]. The identification of the parameters that influence this spatial structure is of particular interest.

First, the colon is the place of complex fluid mechanics: the luminal flow of digestive residuals carries along the colonic content towards its distal part, while the colon epithelium pumps water [3], twisting the stream lines and reducing the transport speed. In the same time, the mucus layer that wraps the epithelium, together with the inhomogeneous luminal content, creates viscosity gradients that further deform the flow [15] while the active contractions of the intestine wall during its motile activity [20] induce additional perturbations. These interacting hydrodynamic and mechanic forces spatio-temporally structure the colon microbiota.

The second parameter impacting the spatial distribution of the microbiota is the nutrient availability. The colon is an anaerobic medium, where the main nutrient sources for microorganisms are undigested dietary fibres or host-derived polysaccharides and their by-products: this constitutes a selection pressure that favors fermentative microorganisms. The polysaccharides degradation is therefore central in the ecological interactions within the microbiota and structures the whole community through trophic exchanges of electron acceptors[11]. The interplay between the microbial populations and their nutritional landscape can be further intricate due to their ability to forage for nutritional sources through active motion: whereas bacterial flagella expression is repressed by the host immune system near the epithelium [9], active swimming is needed for the colonization of several pathogens [11] and low motile activity is observed for commensal bacteria [36].

Finally, the epithelial mucus plays a particular role in the gut microbiota homeostasis and its spatial shape. This viscous fluid insulates the epithelium wall and forms a passive protection against a microbial invasion. But it also provides an additional way for the bacteria to escape the flow of the intestinal content by binding to the mucus layer to prevent their wash out. Furthermore, the mucus represents a source of polysaccharides directly provided by the host: the mucins and their glycans that compose the epithelial mucus can be degraded with the same enzymatic mechanisms as for fibres [16].

Experimental devices mimicking the colonic environment provide highly valuable information [11, 22, 23, 35, 2] on the gut microbiota functioning and its spatial structure. Reductionist approaches on gnotobiotic rodents [37] are also highly valuable tools. However, they only partially mimic the host response or the ecosystem functions, making it difficult to evaluate the relative importance of the factors that shape the spatial distribution of the microbiota. This is why mathematical modeling approaches provide a helpful complement to experiments to gain insight on the main parameters influencing the spatial structure of the bacteria in the colon.

Several models of the gut microbiota were proposed in the literature to study

the spatial structure of the microbial communities. The first model that was introduced [25] emphasized the modeling of the fibre degradation activity, by adapting a model of anaerobic digestion from bioprocess engineering [4]. The space was handled through a rough discretization of the colon into physiological compartments. An improved version of this model, based on an infinite sequence of longitudinal compartments and represented by a one-dimensional partial differential equation was developed in [24]. It assumed a constant flow speed along the colon, reducing the fluid mechanic effects to an averaged retention time. A more sophisticated description of the hydrodynamic transport speed was proposed in [7], together with a diffusive term describing the peristaltic activity of the large intestine assessed by comparison with biophysical experiments [8], and a pH-dependent bacterial activity. The resulting model was unidimensional in space, and the hydrodynamics was reduced to the volume conservation during water absorption, while the gut microbial community was simplified up to a pair of bacterial strains. In [12], an accurate description of the fluid dynamics of the multiphase luminal content was proposed to study the constitution and the turnover of the mucus layer, but the interactions with the microbiota were not studied.

In this paper, we present a new model coupling the fluid mechanics model of the colonic content and the mucus layer introduced in [12] with the metabolic model of bacterial populations presented in [25]. To our knowledge, this model allows for the first time a full study of the spatial distribution of the microbiota including the interactions with its fluid environment. The complexification of the fluid mechanics description allowed to investigate specific features such as epithelial motility, active swimming or the dependency of the local viscosity to the luminal content composition, together with their impact on the fluid streams and the microbiota growth.

2 Material and methods

2.1 Mathematical model of the gut microbiota and its metabolic substrate

We present the mathematical framework, emphasizing the underlying biological assumptions of the model and the modeling of the different mechanisms able to impact the spatial structure of the microbiota.

2.1.1 Geometrical assumptions

The dynamic of the populations and their interaction with the fluid is described by a set of partial differential equations. The equations are set on a cylindrical domain $\Omega = \omega \times [0, L]$ of \mathbb{R}^3 that represents the geometry of the colon, with $\omega \subset \mathbb{R}^2$ its transverse section, which is a disc of radius $R > 0$. We denote by

$$\Gamma_{in} = \omega \times \{0\}, \quad \Gamma_{out} = \omega \times \{L\}, \quad \Gamma_m = \partial\Omega \setminus (\Gamma_{in} \cup \Gamma_{out})$$

the proximal extremity (just after the ileocecal valve), the distal boundary (which is set in the middle of the sigmoid colon, before the rectum) and the mucosal wall of the colon, respectively. Physiological compartments can be defined as portions of the total cylinder: the proximal, transverse and distal

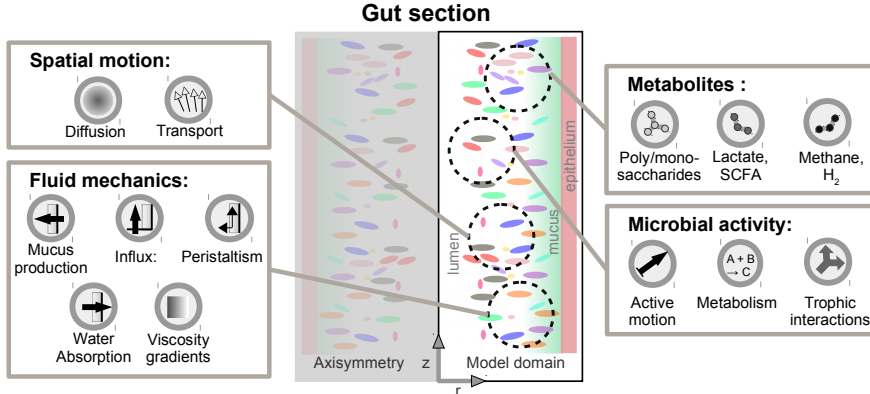


Figure 1: Overview of the different processes considered in the model.

colons have respective length of $0 < L_{prox} < L_{trans} < L_{dist}$, which satisfy $L_{prox} + L_{trans} + L_{dist} = L$. In our approach, the end of the sigmoid colon and the rectal parts are not modeled. More precisely we take $L_{prox} = 21\text{cm}$, $L_{trans} = 70\text{cm}$, $L_{dist} = 63\text{cm}$ such that the total length is shorter than the averaged physiological colorectal length, which is about 190cm [18, 7].

We refer the reader to Table A.4 for the physical values attributed to the geometrical data for the simulations.

2.1.2 Global structure of the model

The model we propose is based on reasonings from mixture theory [28, 6], adapted to the multiphasic intestinal content. We refer the reader to [12] for a first attempt in that direction. Among the different entities considered in this model, we distinguish the mixture components that are large enough to produce mechanical forces, hence impacting the fluid mechanics, and the diffusing compounds dissolved in the intestinal mixture, without any impact on the mixture flow.

As in [25], the model is structured around the fibre degradation. Four functional microbial metapopulations are involved, each acting at different stages of polysaccharides metabolic pathways. The first population, called B_{mon} , hydrolyses the fibres and mucus polysaccharides to produce monosaccharides, that, in turn, are metabolized to support their growth, producing lactate, short-chain fatty acids (SCFA), i.e. acetate, propionate and butyrate, and dissolved gas (H_2 and CO_2). The population B_{la} then grows on lactate and produces SCFA and gas, while the populations B_{H_2a} and B_{H_2m} are fueled by the di-hydrogen, through respectively the homeoacetogenesis and methanogenesis pathways. In order to maintain physiological gas concentration in the liquid, we model vapourisation to gaseous phase. We finally get 13 processes (see Fig. A.1 for a synoptic view of the reactions involved in the model). The different bacterial populations are gathered in the set $I_B = \{B_{mon}, B_{la}, B_{H_2a}, B_{H_2m}\}$. Next, we assume that the largest elements capable to influence the fluid mechanics are the mucus (m), the polysaccharides (pol), the 4 bacteria (described by the set I_B), the liquid chyme (l) and indigestible residuals (r) that are not metabolized by bacteria but do impact the local rheology. We then collect these mixture

components in the 8 elements set $I_C = \{m, pol, B_{mon}, B_{la}, B_{H_2a}, B_{H_2m}, l, r\}$, which thus contains I_B . The dissolved compounds (which include, among other, the gas and SCFA involved in the model) are collected in the set $I_S = \{mon, la, H_2, ac, pro, bu, CH_4, CO_2\}$ for respectively the monosaccharides, the lactate, the hydrogen, the acetate, the propionate, the butyrate, the methane and the carbone dioxyde. We remark that, unlike [25], we do not explicitly introduce a gaseous phase in the model.

In what follows, we are going to describe in details the equations that govern the evolution of volume fractions of the mixture components and the evolution of concentrations of the dissolved compounds. These mass balance equations contain some source terms coming from the metabolic reactions, which involve some transfers of mass from one phase to another. They also include transport terms, with a velocity computed from fluid dynamics considerations and from the bacterial active motion (see Fig. 1 for a global overview of all the mechanisms that are taken into account). To help the reading of the paper, all the model variables and notations are recalled in Table A.2.

2.1.3 Mass conservation equations

As all the phases of the multiphasic colonic content are mainly composed of water, we assume that they all have the same constant mass density ρ . The mixture state is then totally described by the volume fractions f_i of its phases. We model the time evolution of the volume fraction of the component $i \in I_C$ by the following reaction-diffusion-convection equation

$$\partial_t f_i - \operatorname{div}(\sigma \nabla f_i) + \operatorname{div}(f_i u_i) = F_i. \quad (1)$$

When the mixture is at rest, which means when the different transport terms vanish, the phases are supposed to inter-penetrate each other by diffusion, i.e. we assume that the interface forces are not sufficient to maintain a sharp separation of the different phases. We model that feature with the diffusive term $\operatorname{div}(\sigma \nabla f_i)$, a simple Fick's law. For simplification purposes, we assume the same diffusion coefficient $\sigma > 0$ for all phases, but each phase has its own velocity field u_i . The definition of the source term F_i , the metabolic transformation rate of the mixture component i , will be detailed later on. Nevertheless, for modeling issues, it is important to bear in mind that the phase-to-phase transfers embodied into the F_i 's are volume invariant which amounts to assume that

$$\sum_{i \in I_C} F_i = 0. \quad (2)$$

For the derivation of the equations, we are also going to use the fact that the mixture fills up the whole intestinal volume resulting in the following saturation constraint

$$\sum_{i \in I_C} f_i(t, x) = 1, \quad \text{for any } t > 0, x \in \Omega. \quad (3)$$

We equally use reaction-diffusion-convection equations for the dissolved compounds concentrations. However, we assume different diffusion coefficients while the velocity field for the dissolved constituents is defined by the local weighted average of the mixture phase velocities

$$\tilde{u} = \sum_{i \in I_C} f_i u_i \quad (4)$$

(which can be interpreted as the mean volume velocity of the flow). We finally get the following equation for the concentration of the chemical j

$$\partial_t c_j - \operatorname{div}(\sigma_j \nabla c_j) + \operatorname{div}(c_j \tilde{u}) = G_j \quad (5)$$

where $\sigma_j > 0$ and G_j are the diffusion coefficient of the diffusing compound j and its reaction rate, respectively. We emphasize that G_j can gather several reaction rates if the compound j is involved in several reactions (see Table A.1 and section A.1 in the Annexes for further details). The definition of the source term G_j will also be precisely defined later on.

2.1.4 Velocity fields

The convection of each fluid component f_i results from two different phenomena:

- the transport by the carrying fluid, described by the velocity field $(t, x) \mapsto u(t, x)$, the evolution of which is driven by fluid mechanics principles,
- for the bacteria, a correction which is intended to describe an active motion towards metabolite sources. This correction is modeled by a chemotactic velocity $(t, x) \mapsto \vartheta_{i,chem}(t, x)$, see [17, 13].

Therefore, we are led to define the apparent velocity field

$$u_i = u + \vartheta_{i,chem}. \quad (6)$$

Using (3), this gives the following velocity for the dissolved compounds mass equation :

$$\tilde{u} = u + \sum_{i \in I_B} f_i \vartheta_{i,chem}.$$

It remains to detail the equations that govern the evolution of u and $\vartheta_{i,chem}$.

2.1.5 Microbial active motion

We bear in mind that $\vartheta_{i,chem} = 0$ for $i \in I_C \setminus I_B$. However, each bacteria is affected by a chemotactic behavior directed towards their substrate : bacteria B_{mon} is attracted by mucus, polysaccharides and monosaccharides, bacteria B_{la} is attracted by lactate and the populations B_{H_2a} and B_{H_2m} are attracted by dihydrogen.

The active motion are modeled by the Keller-Segel model: the gradient of a chemotactic potential influences the resulting velocity, which is therefore defined as

$$\vartheta_{i,chem} = \sum_j \lambda_{ij} \nabla \Phi_j, \quad (7)$$

where Φ_j is the chemotactic potential created by the metabolite j and $\lambda_{i,j}$ is the chemosensitivity coefficient for the bacteria i and the metabolite j , see [17, 13]. The chemotactic potential of the metabolite $j \in I_S \cup \{m, pol\}$ is defined (up to an irrelevant constant) through the resolution of the Poisson equation with Neumann boundary conditions: with η the unit outward normal vector on $\partial\Omega$, we have, when $j \in I_S$,

$$\begin{aligned} -\Delta \Phi_j &= c_j - \frac{1}{|\omega|} \int_{\omega} c_j(x, z) \, dx && \text{in } \Omega \\ \nabla \Phi_j \cdot \eta &= 0 && \text{on } \partial\Omega. \end{aligned} \quad (8)$$

and, when $j \in \{m, pol\}$,

$$\begin{aligned} -\Delta\Phi_j &= f_j - \frac{1}{|\omega|} \int_{\omega} f_j(x, z) dx && \text{in } \Omega \\ \nabla\Phi_j \cdot \eta &= 0 && \text{on } \partial\Omega. \end{aligned} \quad (9)$$

The term $\frac{1}{|\omega|} \int_{\omega} c_j(x, z) dx$ (resp. $\frac{1}{|\omega|} \int_{\omega} f_j(x, z) dx$), which averages over the transverse section ω , relies on a compatibility condition for Eq. (8) (resp. (9)) to be solvable. It differs from the usual average which involves the whole domain, that is to say $\frac{1}{|\Omega|} \int_{\Omega} c_j(x, z) dx dz$ (resp. $\frac{1}{|\Omega|} \int_{\Omega} f_j(x, z) dx dz$). This modification is motivated by the simplified model that we propose, based on asymptotic arguments, when the aspect ratio of the colon goes to 0, see Section 2.2. In the asymptotic limit, the longitudinal chemotactic forces vanish, and the operator $\Delta\Phi_j$ degenerates into $\frac{1}{r} \partial_r (r \partial_r \Phi_j)$: the chemotactic active swimming occurs in the radial direction only. The term $\frac{1}{|\omega|} \int_{\omega} c_j(x, z) dx$ (resp. $\frac{1}{|\omega|} \int_{\omega} f_j(x, z) dx$) enables us to provide a compatibility condition which applies equally in the asymptotic regime of Eq. (8) (resp. (9)).

2.1.6 Fluid dynamics model

Summing Eq. (1) over $i \in I_C$, together with Eq. (2) and Eq. (6), we get a constraint on the mean volume velocity

$$\operatorname{div} \left(\sum_{i \in I_C} f_i u_i \right) = \operatorname{div}(\tilde{u}) = 0 \quad \text{or, equivalently,} \quad \operatorname{div}(u) = -\operatorname{div} \left(\sum_{i \in I_B} f_i \vartheta_{i,chem} \right). \quad (10)$$

This constraint enables us to write Eq.(5) as follows :

$$\partial_t c_j - \operatorname{div}(\sigma_j \nabla c_j) + \tilde{u} \cdot \nabla c_j = G_j. \quad (11)$$

We end up with a momentum conservation equation: we model the mixture velocity with the following Stokes equation on u

$$\nabla p - \operatorname{div}(\mu D(u)) = 0 \quad (12)$$

where $D(u) = \frac{1}{2}(\nabla u + \nabla u^\top)$ and p is the pressure, that is to say the Lagrange multiplier which ensures the effectivity of the constraint (10). In this expression, μ is the apparent mixture viscosity, which depends on space and time through volume fractions. The definition of the viscosity leads to space inhomogeneities which are crucial for the modeling.

It could be possible to incorporate in the right hand side or in the boundary condition a description of further mechanical effects, that can lead to periodic forces. This raises interesting and delicate modeling issues, addressed for instance in the description of blood flows or respiration flows [26].

2.1.7 Definition of the viscosity.

We assume that the local viscosity is inhomogeneous and depends on the local composition of the mixture. This introduces a strong coupling between the fluid

components and the velocity field. We consider that the main drivers of the local mixture viscosity are the mucus and the liquid chyme volume fractions. We set

$$\mu(x, z, t) = \max(\mu_m(f_m(x, z, t)), \mu_l(f_l(x, z, t))) \quad (13)$$

where μ_m (resp. μ_l) stands for a function describing the mucus rheology (resp. the luminal rheology) and depending on the mucus fraction volume (resp. the liquid volume fraction).

Following [12], we first sketch the highly viscous gel-like mucus layer by defining μ_m as a sigmoid function. A threshold level of mucine $f_{m,thr}$ is defined as a marker of the mucus layer: above this threshold, we consider that the mixture is actually mucus and it is assigned a value close to the mucus viscosity $\mu_{m,max}$. Under this level, the contribution of μ_m to the overall viscosity is close to a small value $\mu_{m,min}$. The transition between both values is tuned by a parameter α_m . Namely, we set

$$\mu_m(f_m) = \mu_{m,min} + (\mu_{m,max} - \mu_{m,min}) \frac{f_m^{2\alpha_m}}{f_{m,thr}^{2\alpha_m} + f_m^{2\alpha_m}}. \quad (14)$$

The luminal rheology is defined in the same way based on the liquid phase l : the more liquid l , the less viscous is the mixture, which leads to

$$\mu_l(f_l) = \mu_{l,max} - (\mu_{l,max} - \mu_{l,min}) \frac{f_l^{2\alpha_l}}{f_{l,thr}^{2\alpha_l} + f_l^{2\alpha_l}}. \quad (15)$$

We choose the parameters of the sigmoidal functions so that the sharp transition between the minimal and maximal values of the viscosity occurs in the interval $(0, 1)$, where the volume densities f_m and f_l belong.

2.1.8 Mass transfers through the boundaries.

The modeling of the mass transfers through the boundaries is a key step since they account for the lumen-epithelium exchanges, which are central both in the fluid dynamics and in the metabolic activity through metabolite absorption and release. The parameter values are gathered in Table A.6.

The normal chemotactic velocity vanishes at the boundaries, and we supplement the mass conservation equations (1) and (11) by the natural Robin boundary conditions:

$$(-\sigma \nabla f_i + f_i u) \cdot \eta = \gamma_{f_i} \quad \text{and} \quad (-\sigma_j \nabla c_j + c_j u) \cdot \eta = \gamma_{c_j} \quad \text{on } \partial\Omega, \quad (16)$$

where η is the unit outward normal vector to the boundary. Note that thanks to the boundary conditions set for the chemotactic potentials Φ_j , see eq.(8) - (9), we have that $u \cdot \eta = \tilde{u} \cdot \eta$ on $\partial\Omega$. It remains to detail the boundary fluxes γ_{f_i} and γ_{c_j} , that model the mass transfers through the boundaries. We distinguish several cases where γ_{f_i} and γ_{c_j} are some constant values, or functions of the space variables, or functions of the phases volume fractions.

We recall here that Γ_{in} denotes the proximal extremity, Γ_{out} the distal extremity of the colon and Γ_m the mucosal wall of the large intestine, that is to say the lateral boundary.

- **Dietary inflow on Γ_{in} .** We introduce a velocity profile $u_{in} = u \cdot \eta$ on Γ_{in} such that its average is equal to $U_{in} = V_{in}/|\omega|$ where V_{in} is the daily volume of digestate that reaches the colon. The dietary inflow of fibres, bacteria and monosaccharides is then defined by the formula $\gamma_{f_i} = U_{in} f_{i,in}$ on Γ_{in} , where $f_{i,in}$ is the component density in the inflow. Similarly, we will set $\gamma_{c_j} = U_{in} c_{j,in}$ on Γ_{in} .

Values U_{in} , $f_{i,in}$ and $c_{j,in}$ are given in agreement with biological observations, see Table A.6. Note that the coefficients $c_{la,in}$, $c_{ac,in}$, $c_{bu,in}$, $c_{pro,in}$, $c_{H_2,in}$, $c_{CH_4,in}$, $c_{CO_2,in}$ are all equal to 0 mol.cm^{-3} .

- **Water pumping through the mucosa on Γ_m .** According to [7], we define the strongest water pumping rate $g_{l,max}$ proximally in the colon mucosa until $z = L_{max,pump}$, followed by a linear diminution of the water uptake until $z = L_{min,pump}$, and finally a smaller basal activity $g_{l,min}$ distally. We define on Γ_m

$$\begin{aligned} \gamma_{f_l} &= g_{l,max} f_l \text{ for } z \in [0, L_{pump}^{max}], \quad \gamma_{f_l} = g_{l,min} f_l \text{ for } z \in [L_{pump}^{min}, L], \\ \gamma_{f_l} &= \left(g_{l,max} - \frac{z - L_{pump}^{max}}{L_{pump}^{min} - L_{pump}^{max}} (g_{l,max} - g_{l,min}) \right) f_l \text{ for } z \in [L_{pump}^{max}, L_{pump}^{min}]. \end{aligned}$$

- **Mucus production on Γ_m .** We consider that the mucosa insures the mucus layer homeostasis by a regulatory mechanism that produces mucus when the mucus level is below a threshold f_m^* and consumes mucus otherwise. We then set on Γ_m

$$\gamma_{f_m} = g_m (f_m - f_m^*)$$

where g_m is the mucus production rate.

On Γ_m , we also set $\gamma_{f_i} = 0$ when $i \in I_C \setminus \{l, m\} = \{pol, r, B_{mon}, B_{la}, B_{H_2a}, B_{H_2m}\}$.

- **SCFA and other compounds absorption on Γ_m .** On Γ_m we impose a linear distribution of SCFA absorption along the mucosal wall between a maximal absorption rate $g_{j,max}$ in the proximal part and a minimal rate $g_{j,min}$ in the distal part, for the SCFA j . We then set

$$\gamma_{c_j} = g_{j,max} - (g_{j,max} - g_{j,min}) \frac{z}{L} \text{ for } j \in \{la, ac, pro, bu\}$$

and

$$\gamma_{c_j} = 0 \text{ otherwise, that is to say for } j \in \{mon, H_2, CH_4, CO_2\}.$$

- **Outflow on Γ_{out} .** Summing the mass conservation equations (1) over $i \in I_C$, taking into account the saturation constraint (3), the volume conservation constraint (2) and the boundary conditions (16), and integrating over Ω shows that

$$\int_{\Gamma_{out}} u \cdot \eta \, d\sigma = \sum_{i \in I_C} \int_{\Gamma_{in} \cup \Gamma_m} \gamma_{f_i} \, d\sigma.$$

In other words, the outflow balances the other mass transfers through the boundaries in order to conserve the overall volume. We then set on Γ_{out} , for all $i \in I_C$, $\gamma_{f_i} = f_i u_i \cdot \eta$ and for all $j \in I_S$, $\gamma_{c_j} = c_j \tilde{u} \cdot \eta = c_j u \cdot \eta$.

2.1.9 Epithelial motility and peristalsis

To close the overall system, it only remains to define boundary conditions for the velocity on Γ_m . We remind the reader η as the local unitary outgoing normal vector, and we denote by η_z the longitudinal tangential unitary vector (that is $\eta_z = (0, 0, 1)$ on Γ_m and $\eta_z = (1, 0, 0)$ on Γ_{out} , in cylindrical coordinates), and $\eta_r = \eta_z \wedge \eta$ the radial tangential unitary vector. Then, we set

$$u_i \cdot \eta = \sum_{i \in I_C} \gamma_{f_i} + U_{per,r}, \quad u_i \cdot \eta_z = U_{per,z}, \quad u_i \cdot \eta_r = 0 \text{ on } \Gamma_m, \quad (17)$$

where $U_{per} = (U_{per,r}, 0, U_{per,z})$ is a velocity profile describing the net motile activity of the mucosal wall, including peristalsis and segmentation contractions.

2.1.10 Metabolic activity

We recall that we model 13 reactions: polysaccharide and mucus degradation (P1 and P2, involving B_{mon} and producing monosaccharide), monosaccharide degradation (P3, involving B_{mon} and producing lactate, SCFAs and gaz), lactate metabolism (P4, involving B_{la} and producing SCFAs and gaz), acetogenesis (P5, involving B_{H_2a}), methanogenesis (P6, involving B_{H_2m}), bacterial death (4 reactions: P7-P10), and gaz vaporisation (3 reactions, P11-P13).

We adopt a matricial formalism to define at the same time the whole set of source function F_i and G_j . We note P_c (resp. P_s) the reaction 8×13 matrix for the mixture components (resp. the solutes) that defines the yield of each process on the corresponding compounds, based on the stoichiometry of the 13 processes [25]. We also introduce the kinetic rate vector $K = (K_p)_{p=P1, \dots, P13}$, which components are defined by $k_p \rho_p$ for the different processes $p = P1, \dots, P13$ under consideration. Finally, with $F = (F_i)_{i \in I_C}$ and $G = (G_j)_{j \in I_S}$, we set

$$F = P_c K \text{ and } G = P_s K. \quad (18)$$

To ensure the volume-conservation condition (2), we consider that mucus or polysaccharides consumption, or bacterial death, releases an equivalent volume of liquid (see volume transfers in Fig. A.1). Conversely, we assume that bacterial growth is limited by the available free space in the liquid phase (see Table A.1 in the annexe for the kinetic rates of each process), and that an equivalent volume of liquid is removed during the growth, in order to satisfy (2). Following [25], an additional pH-dependent-repression is introduced for the methanogens B_{H_2m} through a space-dependent linear pH function $pH(z) := I_{pH,min} + (I_{pH,max} - I_{pH,min})z/L$ and a multiplicative factor $I_{pH}(z)$ applied to ρ_{P6} , where

$$I_{pH}(z) := \exp \left(-3 \left(\frac{pH(z) - I_{pH,high}}{I_{pH,high} - I_{pH,low}} \right)^2 \right) \mathbf{1}_{pH(z) < I_{pH,high}} + \mathbf{1}_{pH(z) \geq I_{pH,high}}$$

The bacteria are assigned a constant death rate. We finally note that, unlike [25], the gaseous phase is not modeled, preventing the introduction of an equilibrium term between the dissolved gas and its corresponding gaseous phase through an Henry law. We then introduce a sink source term $G_j := k_i (c_j - K_{h,P_i} RT [c_{j_g}]_\infty)$, for $j \in \{CH_4, CO_2, H_2\}$ (see also Table A.1b), where $[c_{j_g}]_\infty$ is the asymptotic value of the corresponding gas in the proximal luminal

part of [25], and R and T are the perfect gas constant and the temperature. It is equivalent to define a Henry law with a stationary homogeneous gas phase.

We gather in Table A.1 the precise definition of the reaction matrices and the growth rates. The values for all the parameters Y_{g,P_i} , k_p , K_{h,P_i} , K_{x,P_i} , K_{s,P_i} , $I_{pH,min}$, $I_{pH,max}$, $I_{pH,low}$, $I_{pH,high}$, $[jg]_\infty$, R and T are given in Table A.5.

2.1.11 Units of the model

The time and space values are expressed in day and cm. The mixture components are dimensionless, since they represent volume fractions and therefore F_i should be in day^{-1} . Since we assume that all the phases have the same water density $\rho = 1\text{g}\cdot\text{cm}^{-3}$, the volume fractions can be easily converted to mass densities. To allow comparisons with the usual units of bacterial levels in microbiology literature, such as Colony Forming Units per grams ($\text{CFU}\cdot\text{g}^{-1}$) which is linked to the number of living microbes per mass unit, we assume that the average volume of a single bacteria is $1\mu\text{m}^3 = 10^{-12}\text{cm}^3$. Thus, a direct conversion between bacterial volume fractions and $\text{CFU}\cdot\text{g}^{-1}$ of colonic content can be obtained by applying a multiplicative factor of 10^{12} to the bacterial volume fraction. The densities of the dissolved compounds are expressed in $\text{mol}\cdot\text{cm}^{-3}$. The units of the different model parameters are detailed in Tables A.4, A.5 and A.6.

2.2 Model simplification

For computational purposes, it is interesting to work with a reduced model, which can be obtained owing to scaling reasoning. Using cylindrical coordinates (r, θ, z) , we start by assuming that the state of the system does not depend on the angular coordinate θ . Exploiting the aspect ratio of the colon $\varepsilon := L/R \ll 1$, we formally expand the solutions of (1)-(17) as power series

$$\begin{aligned} f_i &= f_i^{(0)} + \varepsilon f_i^{(1)} + \varepsilon^2 f_i^{(2)} + \dots, \\ c_j &= c_j^{(0)} + \varepsilon c_j^{(1)} + \varepsilon^2 c_j^{(2)} + \dots, \\ u &= u^{(0)} + \varepsilon u^{(1)} + \varepsilon^2 u^{(2)} + \dots \end{aligned}$$

The asymptotics involves the differential operators

$$u = (u_r, u_z) \mapsto \text{div}_r u := \frac{1}{r} \partial_r (r u_r) + \partial_z (u_z)$$

and

$$c \mapsto \nabla_r c = (\partial_r c, \partial_z c).$$

Identifying the leading terms in the expansion and omitting the superscripts for simplicity reasons, we are led to

$$\sum_{i \in I_C} f_i = 1 \tag{19}$$

$$\partial_t f_i - \frac{1}{r} \partial_r (r \sigma \partial_r f_i) + \text{div}_r (u_s f_i) + \frac{1}{r} \partial_r (r \vartheta_{i,r} f_i) = F_i \tag{20}$$

$$\partial_t c_j - \frac{1}{r} \partial_r (r \sigma_j \partial_r c_j) + \tilde{u} \cdot \nabla_r c_j = G_j, \tag{21}$$

where the velocity u_s and the active motion field $\vartheta_{i,r}$ will be detailed below. We note that longitudinal diffusion and chemotactic velocity vanish, because the dimensional analysis reveals that these two contributions are negligible in comparison with the longitudinal transport. From a biological point of view, this is reminiscent to the assumption that the bacteria are not able to swim against the longitudinal flow, but that their active motion capabilities allow them to move along the radial direction.

The active transport velocity $\vartheta_{i,r}$ is given by

$$\vartheta_{i,r} = \left(\sum_j \lambda_{i,j} \Upsilon_j, 0 \right) \quad (22)$$

where Υ_j is computed from the volume fraction f_j or the chemo-attractant concentration c_j with the following explicit formula

$$\begin{aligned} \Upsilon_j(r, z) &= - \left(\frac{1}{r} \int_0^r s f_j(s, z) ds - \frac{r}{R^2} \int_0^R s f_j(s, z) ds \right), \quad j \in \{m, pol\} \\ \Upsilon_j(r, z) &= - \left(\frac{1}{r} \int_0^r s c_j(s, z) ds - \frac{r}{R^2} \int_0^R s c_j(s, z) ds \right), \quad j \in \{mon, la, H_2\}. \end{aligned} \quad (23)$$

The mixture velocity $u_s = (u_{s,r}, u_{s,z})$, solution of the asymptotic version of the Stokes equation, is given by the explicit formulas

$$u_{s,z}(r, z) = - \frac{\Lambda(r, z)}{\kappa(z)} \left(R \int_0^z \sum_{i \in I_C} \gamma_{f_i}(R, y) dy - R^2 U_{z,in} + \frac{R^2}{2} U_{per}(z) \right) + U_{per}(z) \quad (24)$$

$$u_{s,r}(r, z) = \left(- \frac{1}{r} \int_0^r s \partial_z u_{s,z}(s, z) ds - \sum_{i \in I_C} f_i(r, z) \sum_{j \in I_C \cup I_S} \lambda_{i,j} \Upsilon_j(r, z) \right), \quad (25)$$

where

$$\Lambda(r, z) = \int_r^R \frac{s}{\mu(s, z)} ds, \quad \kappa(z) = \int_0^R s \Lambda(s, z) ds, \quad U_{z,in} = \frac{1}{R^2} \int_0^R s \sum_{i \in I_C} \gamma_{f_i}(s, 0) ds.$$

We point out that the velocity field keeps track of the key parameters of the fluid mechanics: the heterogeneity of the viscosity μ , the boundary conditions $\gamma_{f_i}(R, z)$ through the mucosa, the average intake $U_{z,in}$, the peristalsis U_{per} , and the bacterial radial swim through the term Υ . We also note that, taking $u = u_s$ and $\nabla \Phi = \Upsilon$, the volume conservation constraint (10) is preserved by construction, avoiding numerical problems of mass conservation. This approximate model represents a huge reduction of the computational load, with a speed up of about 70, but gives accurate approximations of the initial model.

2.3 Numerical implementation

We solve Eqs. (20)-(21) by a first-order time splitting method, coded in `Matlab` (MathWorks, version R2016b). The code sources can be found at <https://>

`forghemia.inra.fr/simon.labarthe/gut-microbiota.git`. At each iteration, we use a finite volume scheme on a MAC grid, with explicit time integration for the transport term (enforcing the positivity of the solution with a CFL condition) and implicit scheme for the diffusion. The spatial operators are applied alternatively in each spatial direction, which reduces the size of the linear systems to be solved. We end the time loop by integrating the source term with a semi-implicit Euler method that preserves the positivity. Namely, the negative contributions of the source function are passed on the left hand side and solved semi-implicitly, while the positive contributions are kept in the right-hand side and treated explicitly [27]. The implicitation of the negative term does not involve any linear system inversion: due to the multilinear form of the different terms of the source function, the matrix to be inverted is diagonal. We note that we take advantage of the equation $\sum_{i \in I_C} f_i = 1$ to avoid solving the equation on f_l by taking $f_l = 1 - \sum_{i \in I_C, i \neq l} f_i$. The model parameters can be found in Table A.4 for the parameters related to diffusion, speed and initial conditions, in Table A.5 for the parameters of the source function and in Table A.6 for the boundary conditions.

2.4 Strategy of the numerical experiments.

To colonize the colon, the microbial populations have to face the flow of the intestinal content. Several mechanisms have been identified as possible drivers of the microbial populations spatial distribution[7] such as 1) the polysaccharide level shaping the overall microbial population 2) the mucus zone providing nutrients and protecting the microbial populations from the luminal flow, 3) bacterial active swimming possibly favoring bacterial persistence, 4) epithelial motility, through peristalsis or segmentation contraction, slowing down the flow and helping maintaining the microbes in the colon.

In order to separate the different mechanisms, we first define a basal reference condition for comparison: we knock down the peristalsis and the chemotactic activity, and select a polysaccharide input (20 g.day^{-1}) representative of a normal reference diet. We then perform a long time simulation, starting from the mucus volume fraction equal to f_m^{init} , the liquid volume fraction equal to $f_l^{init} = 1 - f_m^{init}$ and the other volume fractions $f_i^{init} = 0$, for all $i \in I_C, i \neq l, m$. The mucus initial condition f_m^{init} is given by a sigmoid function, following [12], that distributes the mucus level from $f_{m,min}^{init} = 0$ in the lumen to $f_{m,max}^{init}$, the physiological amount of mucins in the mucus layer. We set

$$f_m(0, r, z) = f_m^{init}(0, r) = f_{m,max}^{init} + (f_{m,max}^{init} - f_{m,min}^{init}) \frac{r^{2\alpha_m^{init}}}{r^{2\alpha_m^{init}} + r_m^{2\alpha_m^{init}}}$$

where r_m is a threshold defining the average thickness of the mucus layer. This simulation is conducted until steady state, that is further used as a reference state. We check that this reference state can be taken as a proxy of a healthy gut microbiota, by verifying that key markers are recovered in a physiological range (see the Results section). This reference state is taken as the initial condition of the additional numerical experiments, that are conducted until a new steady state is reached. This final state is compared to the reference initial state to assess the outcome of the experiment.

We next check the impact of the four putative mechanisms separately, by modifying only the model parameter that corresponds to the given mechanism. 1) The effect of dietary fibre is assessed by increasing or decreasing the fibre intake by 30%. 2) The effect of the mucus zone is checked in two different ways: in order to test if the nutrients provided by the mucus layer strongly shape the microbiota, we first knock down the mucus metabolism in the B_{mon} population. As the mucus layer strongly impacts the local rheology, we next remove the viscosity heterogeneity by taking a homogeneous viscosity map, to check if the rheology discrepancies in the colon have an effect on the spatial repartition. 3) The chemotactic function is introduced by setting a chemotactic speed with characteristic value 1cm day^{-1} , which is small comparatively to the transit speed. 4) The peristalsis is checked by applying an upstream peristaltic speed by setting $U_{per,z} = -10\text{cm day}^{-1}$. The parameters used in the simulations can be found in Tables A.4, A.5 and A.6.

2.5 Sensitivity analysis.

We perform a sensitivity analysis of the model outputs to parameter variations around the parameters identified in the previous simulations. We aim at testing the impact of selected parameters on the bacterial distribution. Namely, we select the epithelial motility ($U_{per,z}$ parameter), the bacterial chemotaxis (λ_{ij} parameters, that are modified in the same proportion), the viscosity gradient ($\mu_{max,m}$ and $\mu_{max,l}$ parameters, that are shifted together) and the fibre intake ($f_{pol,in}$ parameter). We study the variations of the output $B(z) = \sum_{i \in I_B} \frac{2}{R^2} \int_0^R rc_i(r, z) dr$ when varying the selected parameters. We build a total factorial design by allowing for each parameter θ five levels corresponding to 50, 80, 100, 120 and 150% of its nominal value θ_0 introduced in Tables A.4, A.5 and A.6. Testing 4 parameters results in a design containing 625 different sets of parameter values and the same number of model runs to perform the sensitivity analysis. The model outputs are post-processed with the R package Multisensi (<https://CRAN.R-project.org/package=multisensi>). We compute with Multisensi the descriptive statistics on $B(z)$, the distribution of the first order Sobol index of each parameter along the colon length with the method introduced in [19], see Fig 9. We recall that the first order Sobol index $S_\theta(z)$ of a given parameter θ , for a given $z \in (0, L)$ reads

$$S_\theta(z) := \frac{Var(\mathbb{E}(B(z)|\theta))}{Var(B(z))}.$$

3 Results

We first check that the reference state reproduces the results introduced in [25] and [24] (subsection 3.1). We next assess the effect of diet variations (subsection 3.2.1), viscosity gradient and mucus metabolisms (subsection 3.2.2), peristalsis and active motion (subsection 3.2.3) on the spatial structure of the colonic content. We finally compare the relative influence of each mechanism in the multifactorial process leading to the space repartition of the colon microbiota (subsection 3.2.4) through a sensitivity analysis of the model.

3.1 Characterization of the reference state

We check that the reference state represent a correct proxy of the homeostatic state of the gut microbiota, reproducing physiological markers of the structure and function of a healthy microbiota in the colon. We remind that the motile activity of the epithelial wall and the bacterial active swimming are turned-off in this reference state (i.e. $U_{per} = (0, 0, 0)$ and $\lambda_{ij} = 0$ for all $i \in I_B, j \in I_S \cup \{m, pol\}$) to allow comparison with previous studies [25, 7], and to provide a negative control for these effects.

3.1.1 Longitudinal structure of the colon in the reference state.

The longitudinal distribution of several parameters driving the fluid mechanics and the overall microbial steady-state levels are displayed in Fig. 2. We can see (Fig 2 A, blue line) that the averaged longitudinal speed decreases strongly in the proximal and transverse sections, where the pumping activity by the mucosa is maximal (yellow curve, Fig 2-A). It then reaches an average speed of 4.03cm d^{-1} , which corresponds to an outgoing flux of 169mL d^{-1} , in the range of natural water excretion in faeces ($100\text{-}200\text{mL d}^{-1}$ [14]). The radial speed reaches its highest level at the beginning of the colon and then drops off in the distal part to negligible values. The radial transport is thus expected to dominate over the radial diffusive process in the proximal colon, while the dominance ratio is reversed distally.

A key parameter for the speed dynamics is the viscosity distribution. We can observe (green curve, Fig 2-B) that the viscosity of the colonic mixture increases all along the colon until reaching a maximal value in its distal part before a slight decrease, due to mucus consumption by the microbiota. The viscosity increase reflects water absorption and the resulting concentration of the other mixture components. The microbial activity (red curve, Fig 2-B), defined as the sum over bacteria of the growth and death rates, is mostly driven by the polysaccharides metabolism. The fibres start accumulating in the proximal colon, under the effect of a strong water pumping in this compartment (blue curve, Fig 2-B). They are next entirely consumed by the microbiota in the transverse colon, consequently increasing the microbial activity that reaches its maximum value in the early distal compartment. Then, the microbial metabolic activity drops off until a plateau phase that corresponds to the mucus degradation only. The microbial density (magenta curve, Fig 2-B), first distributed exponentially in the first part of the colon, displays a slope break in the distal part reflecting the metabolic switch from dietary fibres to mucus. The total bacterial volume fraction at the colon exit is $6 \cdot 10^{-2}$, which corresponds to a bacterial density of $0.6 \cdot 10^{11}\text{CFU g}^{-1}$ of faeces, within the range of observed data [31]. Furthermore, the total mass of the gut microbiota is 86g and the total number of bacteria is $8.6 \cdot 10^{13}$, which correspond respectively to half and twice the measured bacterial levels reported in [31].

3.1.2 Spatial distribution of the microbiota and SCFA in the reference state.

The averaged values presented in Fig.2 provide an accurate view of the longitudinal distribution but do not render the radial repartition of the colon content. We then display the distributions in six compartments formed by the luminal

and mucosal parts of the proximal, transverse and distal colons (Fig 3). We can observe that the microbial populations levels are higher in the mucosal part of the proximal and transverse compartments, but lower for the SCFAs. This is mainly the result of the important water absorption in these compartments, which tends to accumulate the mixture components near the mucosa, including the bacteria. On the contrary, the absorption of SCFAs by the mucosa lowers the fatty acids levels in the mucosal part. In the distal part, where the mixture diffusion and the radial speed balance, the microbial distribution is much more homogeneous. Due to absorption, the SCFAs are still depleted distally near the mucosa.

The microbial levels reflect the trophic interactions: the top bacteria in the trophic chain, i.e. the poly/monosaccharides consumers B_{mon} , are also the most present in each compartment. Their level reaches approximatively twice the level of the lactate consumers B_{la} , which in turn is greater than the acetate producers $B_{H_2,a}$ (Fig. 3). The methanogens $B_{H_2,m}$, which are repressed by the increasing pH along the colon, present smaller levels. The complete distribution maps (Fig. B.1, supplementary materials) show that there is a correspondence between these trophic interactions and the spatial distributions: the higher is the bacterial position in the trophic chain, the more proximal is the population repartition front. We also observe that the bacterial populations are higher in the vicinity of the mucus layer and lower in the lumen, reproducing a phenomenon recently observed in vivo by fluorescence imaging with labelled microbial strains [37].

The millimolar ratio Acetate:Propionate:Butyrate in the luminal compartments are 82:41:43 in the proximal part, 74:37:37 in the transverse segment and 57:28:29 in the distal colon, in agreement with the predicted values in [25] and with the experimental measurements in [34, 10]. The overall levels of SCFA in the transverse lumen are over-estimated by our model compared to experimental post mortem measures in this compartment (560 vs 118mM). However, in the mucosal transverse (121 predicted vs 105mM measured) and in the distal compartments (103 vs between 72.4 and 87.5mM measured), the model is in good agreement with experimental data [34, 10].

3.1.3 Mucus layer

In our model, the mucus is represented by the mucin density, which impacts the mixture viscosity through the mucus viscosity function μ_m . Indeed, as the sigmoidal function μ_m is very stiff, the viscosity threshold $f_{m,thr} = 0.0425$ represents the limit of the mucus layer. When the mucus density is above this threshold, we will consider that the corresponding spatial point is inside the mucus layer. At steady state, the mucus layer has a minimal thickness of about 1.7mm in the proximal colon (Fig 4), where the microbial populations are small and the radial speed is high due to water absorption. In the transverse colon, the mucus layer is thicker (4.3mm as maximum) due to the diffusive process that counterbalances the radial transport in that region. In the distal part, the mucus layer is consumed by the microbial populations, after the integral consumption of the fibres, and gets thinner again until reaching 2.4mm. Human data for the mucus thickness are currently lacking in the bibliography [15]. In rats, the total mucus layer thickness (including the firmly and loosely adherent layers) are respectively 0.480 and 0.829mm at the end of the ileum and in the colon

[1]. The colon radius in rats is 0.4cm [21]. Assuming that the rheological and hydrodynamical parameters are the same in rats, a simple rescaling of our model outcome would give a maximal mucus thickness of 0.272, 0.688 and 0.384mm in the proximal, transverse and distal colon, which is comparable to the rat data.

3.2 Study of the drivers of the gut microbiota spatial structure

The reference state is perturbed by modifying a single mechanism included in the model. The consecutive steady state is compared to the reference to assess the importance of the corresponding parameter in the homeostatic regulations. To check the significance of the observed variations, we first check that the reference state is robust respectively to the initial condition: when the initial condition is chosen randomly, the resulting steady-state is quasi-identical to the reference state (relative difference less than 0.1% in L^∞ norm).

3.2.1 Spatial perturbations induced by diet variations.

We assess the outcome of diet variations on the overall dynamics of our model: starting from the reference state, we impose low and high-fibre diets by respectively decreasing or increasing the averaged polysaccharide daily input by 30%, until a new steady-state is reached. We plot in Fig. 5 the speed variations induced by the diet changes, and the modification of the key parameters that were defined in Fig. 2. We observe (Fig 5, A-B) that the longitudinal speed slightly decreases or increases with the fibre intake, which is consistent with the fact that more fibres shorten the transit time in the colon. In our model, these discrepancies are directly related to the modeling of water absorption: in the high-fibre diet, more fibres accumulate near the epithelial wall, leading to less water available for absorption. This enhances the water density in the lumen and consequently, the chyme fluidity and the transit.

The differences in fibre intake impact the fibre distribution in the proximal colon (blue curves, Fig 5, C-D). The fibre concentration increases with the fibre intake, and the fibre distribution is spread out when more fibres are ingested. This is reflected in the microbial activity distribution (red curves, Fig 5, C-D), which presents a shift of the peak activity towards the distal part for higher fibre diets. The microbial densities (magenta curves, Fig 5, C-D) in turn reflect these spatial discrepancies of microbial activity: the microbial density is first slightly higher in the transverse colon for low-fibre diet, but the tendency is rapidly reversed from the beginning of the distal bowel. The overall microbial density is higher for higher-fibre diets, as expected. Conversely, the viscosity distribution (green curves, Fig 5, C-D) is only slightly modified by the diet variations.

Differences in microbial and SCFA densities can also be observed in all the colon compartments (Fig. B.2, supplementary data). The microbial and SCFA levels are directly linked to the quantity of dietary fibres: high-fibre diets enhance the gut microbiota function by increasing the SCFA levels, in accordance with experimental studies [10]. The microbial levels are first equivalent for all diets in the proximal regions but noticeable differences are observed in the distal parts.

3.2.2 Microbes-mucus interactions: mucus-induced viscosity gradients promote the bacterial growth

Due to the ecological importance of the mucus layer, we study the mechanisms that drive microbes-mucus interactions in the model, namely the mixture viscosity and the mucus degradation by the microbiota. We perform a simulation without viscosity gradient by setting a homogeneous mucus function with a median value of $35 \cdot 10^3 \text{ g cm}^{-1} \text{ d}^{-1}$, and a simulation without mucus metabolism by the B_{mon} population, that we compare with the reference simulation (Fig. 6). As expected, the knock out of the mucus metabolism only very slightly alters the speed fields (Fig. 6 A, where the curves are superimposed with the reference state). But the longitudinal speed is significantly reduced due to a higher water absorption in the proximal colon, when the viscosity is homogeneous (blue curve, Fig. 6 B).

A reduced longitudinal speed, by enhancing the retention time, usually promotes bacterial growth. However, the bacterial activity and the overall bacterial populations are drastically reduced (a 60% decrease comparatively to the reference) in the absence of viscosity heterogeneities (red and magenta curves, Fig. 6, D). These discrepancies can be explained by a viscosity-dependent slowdown zone near the mucosa. When the viscosity is mixture-dependent, the mucus layer increases the viscosity gradients, which reduces the longitudinal speed near the mucosa. This deceleration, noticeably marked in the proximal part (dashed blue lines, Fig B.3, B, Supplementary Materials), enhances the local retention time and promotes matter accumulation near the mucus layer, reducing water absorption and increasing water availability for bacterial growth. When the viscosity is homogeneous, a reversed mechanism occurs, promoting water absorption, which results in a reduced bacterial growth due to volume saturation. The identification of the vicinity of the mucus layer as a slowdown zone favoring the bacterial growth is consistent with recent experiments that identified higher bacterial concentrations near the mucus layer in rodents[37].

The suppression of the mucus degradation only slightly modifies the overall dynamics in the proximal part of the colon, but has a sensitive impact in the distal bowel (Fig. 6, C). In this portion of the digestive tract, there are no dietary fibre left, and if the microbial populations are not able to metabolize the host-derived polysaccharides, the bacterial mortality is the preponderant component of the microbial activity. The overall population levels are therefore reduced in the distal part compared to the reference model. However, they are still more than 50% higher than when there is no viscosity gradient (Fig. 6, C-D), suggesting that, in our model, the preponderant mucus-microbes interaction for bacterial growth is the local hydrodynamics near the mucosa induced by the rheology of the mucus layer.

3.2.3 Strong effect of epithelial motility and bacterial active swimming on the spatial structure.

We next investigate the effect of epithelial motility and bacterial active swimming on the overall spatial structure of the colonic content. We reproduce the reference simulation with a constant peristaltic value of $U_{per,z} = -10 \text{ cm day}^{-1}$ for $5 < z < 155 \text{ cm}$ (and $U_{per,r} = 0$), representing the net effect of the peristaltic and segmentation contractions of the colon wall as a upstream flow near the

mucosa[20]. The peristalsis is turned off near the boundaries $z = 0$ and $z = L$ in order to preserve the consistency of the boundary conditions. We next modify the reference simulation by endowing the microbial populations with slight active swimming capabilities by setting for the bacteria i the chemosensitivity $\lambda_{ij} = 1/Grad_{max,j}$ where $Grad_{max,j}$ is the maximal value of the gradient of the chemotactic potential determined by the chemoattractant j in the reference state. The characteristic value of the chemotactic speed is then 1cm day^{-1} , several orders of magnitude under the longitudinal characteristic transit speed (100cm day^{-1}) and the maximal speed observed for the bacterial swimmers, also about 100cm day^{-1} [7]. We remind –see Material and Methods, section 2.2– that the active swimming in the longitudinal direction can be neglected: we then only consider the radial direction of the bacterial motility in the model. The microbial populations included in the model have therefore no possibility to swim upstream against the intestinal transit.

We can observe (blue curve, Fig 7,A) an important increase of the averaged longitudinal speed when the epithelial motility is active, which is counter-intuitive, since the peristaltic activity is applied in the upstream direction. This increase comes from a redistribution of the longitudinal speed along the colon radius. Upstream speeds are observed near the epithelial wall in the peristaltic case, versus null speeds for the reference and the chemotactic experiments, resulting in a large increase of the longitudinal speed in the luminal part to preserve the volume (see Fig. B.4,A-B, Supplementary materials and its legend for details on volume conservation). The radial speed and the mucosal flux are rather similar to the reference state (yellow and red lines, Fig. 7, A) except on the peaks at $z = 5\text{cm}$ and $z = 155\text{cm}$ which correspond to velocity discontinuities at the limit of application of the peristaltic activity. Regarding the speeds components, the chemotactic activity of the bacterial has a very little impact (Fig 7,B and Fig. B.4,B-D).

As expected, the epithelial motility induces a strong upstream shift of the microbial populations, enhancing the bacterial functional activity in the upper transverse colon and promoting a fast consumption of the fibres in the proximal colon (magenta, red and blue curve, Fig 7,C). The bacterial active swimming also promotes the bacterial levels proximally but with smaller magnitude (magenta red and blue curves, Fig 7,D). However, the bacterial metabolism is noticeably boosted in that case, speeding up the carbohydrate consumption, comparatively to the reference simulation (red and blue curves, Fig 7,D). The viscosity (green curves, Fig 7,C-D) is strongly impacted by the epithelial motility, which is related to local modifications on the mucus distribution, but not by the bacterial active motion. We can observe that the wall motility has a focal impact on the overall microbial populations, with a massive increase in the proximal colon and a lower increase at the end of the distal intestine, whereas the enhancement of the bacterial levels are more regular along the colon after activation of the chemotactic capabilities (magenta curves, Fig 7,C-D). We emphasize that very low motile capabilities toward the mucosa, with no longitudinal upstream swimming included in the model, are sufficient to get this positive impact on the total microbial densities.

3.2.4 Deciphering the multifactorial process of spatial structure with sensitivity analysis

We now check that the previous mechanisms result in a positive outcome when combined, i.e., that their respective effects do not compensate each other resulting in a null net effect on the colonic content composition. We can observe (blue line, Fig. 8) that the polysaccharide density drops down very early in the colon, while the bacterial activity reaches its maximal value in the proximal colon. The viscosity is globally reduced, but conserves its increasing profile along the large intestine. The bacterial populations start growing at the beginning of the proximal colon, which is a strong improvement comparatively to the reference experiment where the microbial colonization was effective at the early distal colon only. At the end of the distal bowel, the overall bacterial levels are increased up to 50% compared to the reference.

A more accurate study is performed through a global sensitivity analysis of the different parameters. We shift conjointly the parameters defining the mixture viscosity, the epithelial motility intensity, the bacterial swimming magnitude and the fibre input to assess their impact on the overall bacterial repartition along the colon. Namely, we study for each $z \in (0, L)$ the variations of the radially averaged total bacterial population $B(z)$ (defined in Sec. 2.5) when varying the parameters. We can check in the upper panel of Fig. 9 that the outputs are quite dispersed around the median (bold black line): large differences are observed between extremal values (dashed red lines), and the bandwidth between the second and third quartiles (grey zone) represents about 20 % of the median value in the middle of the colon.

The lower panel displays the Sobol index $S_\theta(z)$ of the different parameters θ that were tested, for $z \in (0, L)$, i.e. the contribution of a given parameter to the total variance of the model outputs. We can observe that the epithelial motility is the main driver of the spatial structure of the bacterial populations in the proximal colon while the level of fibre input is preponderant in its distal part. In the transverse colon, bacterial active swimming and fibre level impacts are equivalent, and the influence of the chemotactic capabilities of the bacteria is noticeable all along the colon, until the very distal part, where diffusion reduces the chemotactic potential gradients. The effect of viscosity variation is very small, with a peak in the very proximal track. This indicates that, despite the necessity of viscosity gradients to obtain physiological bacterial levels (see subsection 3.2.2 above), the discrepancies between higher and smaller viscosity values are not determinant for the microbial growth: the preponderant mechanism could therefore be related to threshold effects in the sharp distribution of the viscosity values near the mucosa, rather than the effective values of viscosity in the lumen and in the mucus layer.

4 Discussion

4.1 Modeling the gut microbiota in its environment

Several models of the gut microbiota were proposed in the literature to study the spatial structure of the microbial communities. The present model couples several modeling frameworks that were previously introduced: it adapts the metabolic model presented in [25] to the fluid mechanics model of the mucus

and the colonic content defined in [12], while taking into account hydrodynamics balances that were thoroughly studied in [7]. Our spatialization strategy can be compared to the method presented in [24], which was a unidimensional spatialization of [25], but we went deeper into details in the description of the fluid dynamics of the colonic content and we also considered 3D phenomena that can occur in the radial direction of the colon. To our knowledge, the present study introduces the first model that considers the interactions of the gut microbiota with its fluid environment by explicitly coupling a population dynamic model of the microbiota and the key luminal metabolites to a fluid dynamic model of the intestinal flow. This modeling platform is a suitable framework to study the spatial structure of the microbiota and the interactions of the bacterial populations with their environment. As the spatial features are of particular interest during pathogen colonization, this model can be notably adapted to study the spatial host-microbiota-pathogen interactions during infection.

4.2 Model improvements

Several limitations of our approach can be underlined. First, the description of the bacterial metabolic activity is reduced to a compact version of the fibre degradation pathways leading from carbohydrates to the main end products: lactate, SCFA and gas. This model is built from prior knowledge of fibre degradation and focuses on the metabolism of the main source of substrate in the colon: carbohydrates. But it neglects other secondary processes. Other metabolic activities are activated, such as bile acid degradation or iron sequestration, that could have a significant importance in the spatial structure of the bacterial populations. Some important abiotic parameters were neglected, such as the redox balance or the complex acido-basic reactions that modify the pH. If needed for a specific study, the metabolic pathways of our model can be supplemented by additional processes of interest, in a case-by-case basis.

Secondly, several biophysical mechanisms of spatial structuration were ruled out. To face the luminal flow, the bacterial communities can express specific phenotypes. Bacterial aggregation or chains formation may be a collective behavior that was selected for enhancing the friction forces and increasing the retention times in the colon. Several bacteria are also able to bind to materials trapped in the mucus layer, such as DNA strands or lysate residuals: this ability allows them to grow near the carbohydrates incorporated in the mucus which gives them a competitive advantage. These behaviors were not modeled in this study, but can be addressed with classical aggregation models such as Smoluchowski equations, or by adding additional friction terms in the moment conservation equation (12). Furthermore, we did not consider periodic features such as post-prandial influx or defecation that could impact the overall dynamics: a more detailed modeling of the fluid mechanics should be introduced to integrate these features.

Finally, if the outputs of the reference model are in the range of observed data, some differences remain: the simulated total microbiota mass at the gut end is half the observations in feces but the simulated total number of bacteria is twice the experimental measures. These discrepancies may reflect the important simplifications that we used in modeling the microbiota. From a metabolic point of view, focusing on fibre metabolism only would lead to underestimate bacterial growth and consequently the overall bacterial levels. Moreover, we

do not model the final part of the colon but the colonic content desiccation through water absorption is still active in the sigmoid compartment, which mechanically increases the microbial concentration. This mechanism could account for the discrepancies between our numerical predictions at the gut end and the measured bacterial concentration in faeces. Furthermore, the bacterial phases are considered in our model as a homogeneous mixture of liquid and bacteria that form at a macroscopic scale a viscous fluid: the derivation of bacterial densities expressed in g cm^{-3} or CFU.g^{-1} then relies on assumptions on the average bacterial volume or on the volume saturation by the bacteria in the bacterial phase, which are questionable when modeling bacterial communities with diverse individual shapes and volumes. These modeling issues could be addressed by developing microscale models of the bacterial communities that could be upscaled through mathematical methods such as homogenization in order to better control these approximations.

4.3 Suitable data for model assessment

Linking outputs of spatial models of the gut microbiota to experimental data for assessment or inference purposes is challenging, due to the gap that still remains between the modeled entities and the biological observations. Invasive data can be collected post-mortem: SCFA or bacterial levels [34, 10] were measured in some points of the colon, but with very coarse spatial accuracy. The mucus layer thickness was also investigated in rodents [1], revealing the difficulty to clearly identify the loose and the firm mucus layers [15]. Furthermore, the very invasive experimental settings prevented until now the same type of studies in humans [15]. These data can be used for a qualitative model calibration, but must be supplemented for parameter inference or quantitative studies.

Omic data can be produced from stool samples, reflecting the state of the gut system at its end: metagenomic data give an insight in the microbial composition of the microbiota and in its functional potential. Metatranscriptomics and metabolomics provide information on the effective expression of microbial functions. In the present study, we could compare levels of specific metabolites, such as SCFA, to measurements in different colonic compartments, or overall bacterial levels. But we have no way to directly link the bacterial levels predicted by our model to metagenomic data, because the modeled bacterial densities are not indexed to any counts of genomic markers. It would be necessary to provide a set of marker genes associated to the different functional populations involved in our model. These marker genes could be a set of *16s* genes detailing the taxonomic composition of the functional populations that could be compared to *16s* counts from stool samples. They could also be a set of genes characterizing the metabolic functions of the functional populations, that could be compared to the corresponding gene counts in shotgun metagenomic data.

Assessing experimentally the spatial structure of the microbiota implies the production of spatial images of the microbial and metabolite distribution. An experimental setup was recently developed [37] in order to track the spatio-temporal evolution of a simplified microbiota of 15 bacterial strains, labelled with a different dye for imaging purposes, and covering the main part of the functions observed in a healthy microbiota. This kind of data set is very promising for assessing spatio-temporal model of the gut microbiota. However, it would need again to modify the structure of the model in order to fit with the specific

bacterial populations involved in the experimental study.

4.4 Main drivers of the spatial structure of the gut microbiota

In [7], the balance between bacterial growth and bacterial dilution by the convection was carefully studied, in order to identify a range of colonic content flow allowing bacterial colonization. The authors argued that the hydrodynamics alone was not sufficient to reduce the apparent speed in the colon under the dilution threshold, which is a necessary condition for bacterial growth. Several biological mechanisms capable to enforcing the speed reduction or enhancing the retention time were thoroughly discussed and peristalsis was identified as the preponderant mechanism that supplements the hydrodynamics to enable the settlement of bacterial communities.

In the present study, additional fluid mechanic effects were introduced, such as viscosity heterogeneities that provide low speed zones near the epithelium resulting in the creation of favorable niches in the mucosa vicinity where the local dilution rate is lower than the bacterial growth. We emphasize that such favorable zones were recently observed by imaging a simplified microbiota composed of 15 labelled bacterial strains: high bacterial concentrations were observed in the surroundings of the mucosal wall, but outside the outer mucus layer [37]. Viscosity heterogeneities in themselves were sufficient to supplement the basal hydrodynamics in order to make bacterial colonization possible. Additional effects, such as epithelial motility or bacterial active swimming, counter-balance the dilution by the fluid flow and consolidate the bacterial levels in the colon. We thus identified a multifactorial process that includes fluid rheology, peristalsis and active swimming, that leads to the constitution of ecological niches in the fluid colonic environment. However, the sensitivity analysis of our model identified the fibre input as the main driver of the microbiota spatial structure, except in the proximal part, where the epithelial motility is determinant for the colonization of the proximal colon. The variations of viscosity gradients weakly impact the bacterial distribution, but an homogeneous viscosity drastically drops down the bacterial populations. This indicates that viscosity heterogeneity is constitutive of a physiological level of bacterial populations, but that the magnitude of these heterogeneities is not preponderant comparatively to the other processes. Threshold effects in the viscosity map near the mucus layer could be the main ingredient of this observation.

Active swimming is often discarded as a possible mechanism enhancing bacterial colonization in the colon, with the arguments that 1) metaproteomic screening of the gut microbiota showed that flagella expression achieved very low levels [36], 2) the maximal known active swimming speeds are in the same order of magnitude as the luminal longitudinal fluid flow, meaning that the bacteria should continuously swim at their maximal capability in order to counter-balance the luminal streams [7], 3) the flagellin is targeted by the host immune system near the epithelium [9]. However, our model showed that very low active swimming (with velocities two orders of magnitude under the longitudinal flow of colonic content) is enough to noticeably enhance the bacterial levels in the large intestine and structure the microbial communities. It is even the main driving process of the bacterial spatial distribution in the transverse colon, together with fibre level. Our model suggests that the active swimming could be

used not to directly face the strong longitudinal streams, since the chemotactic transport in the longitudinal direction is neglected in our model, but to reach the favorable niches near the mucosa.

5 Conclusion

We introduced a continuous spatio-temporal model of the gut microbiota, that couples a population dynamics model of functional populations involved in a trophic chain related to fiber degradation to a fluid mechanics model of the colonic content. A mathematical simplification allowed to reduce the computation time by a factor 70 while keeping the main features. This model was used to investigate the mechanisms driving the spatial distribution of the colonic content and of the microbial populations in the colon. We tested the relative impact of epithelial motility, bacterial active swimming and diet variations through a sensitivity analysis of our model, identifying the later as the preponderant driver of the spatial structure except in the proximal colon, where peristalsis is the main effect, and in the transverse colon, where chemotaxis has an equivalent impact. We observed that very low active swimming capabilities are enough to favor the bacterial growth, indicating that this mechanism should not be discarded from spatial studies of the gut microbiota. We furthermore exhibited a new mechanism involved in bacterial persistence in the colon, based on radial gradients of viscosity that induce the creation of slow stream zones near the mucosa that can be considered as favorable spatial niches in the vicinity of the mucus layer.

Acknowledgments

This publication has been written with the support of the AgreeSkills+ fellowship programme which has received funding from the EU's Seventh Framework Programme under grant agreement Number FP7-609398 (AgreeSkills+ contract).

References

- [1] C Atuma, V Strugala, A Allen, and Lena Holm. The adherent gastrointestinal mucus gel layer: thickness and physical state in vivo. *American Journal of Physiology-Gastrointestinal and Liver Physiology*, 280(5):G922–G929, 2001.
- [2] Elvira Barroso, Carolina Cueva, Carmen Peláez, M Carmen Martínez-Cuesta, and Teresa Requena. Development of human colonic microbiota in the computer-controlled dynamic simulator of the gastrointestinal tract simgi. *LWT-Food Science and Technology*, 61(2):283–289, 2015.
- [3] Gabrio Bassotti and Edda Battaglia. *Physiology of the Colon*, pages 43–53. Springer International Publishing, Cham, 2017.
- [4] Damien J Batstone, J Keller, Irimi Angelidaki, SV Kalyuzhnyi, SG Pavlostathis, A Rozzi, WTM Sanders, H Siegrist, and VA Vavilin. The

- iwa anaerobic digestion model no 1 (adm1). *Water Science and Technology*, 45(10):65–73, 2002.
- [5] R. Chatelin. *Numerical methods for 3D Stokes flow: variable viscosity fluids in a complex moving geometry; application to biological fluids*. Phd thesis, Université Paul Sabatier - Toulouse III, November 2013.
- [6] F. Clarelli, C. Di Russo, R. Natalini, and M. Ribot. A fluid dynamics model of the growth of phototrophic biofilms. *J. Math. Biol.*, 66(7):1387–1408, 2013.
- [7] Jonas Cremer, Markus Arnoldini, and Terence Hwa. Effect of water flow and chemical environment on microbiota growth and composition in the human colon. *Proceedings of the National Academy of Sciences*, page 201619598, 2017.
- [8] Jonas Cremer, Igor Segota, Chih-yu Yang, Markus Arnoldini, John T Sauls, Zhongge Zhang, Edgar Gutierrez, Alex Groisman, and Terence Hwa. Effect of flow and peristaltic mixing on bacterial growth in a gut-like channel. *Proceedings of the National Academy of Sciences*, page 201601306, 2016.
- [9] Tyler C Cullender, Benoit Chassaing, Anders Janson, Krithika Kumar, Catherine E Muller, Jeffrey J Werner, Lergus T Angenent, M Elizabeth Bell, Anthony G Hay, Daniel A Peterson, et al. Innate and adaptive immunity interact to quench microbiome flagellar motility in the gut. *Cell host & microbe*, 14(5):571–581, 2013.
- [10] JH1 Cummings, EW Pomare, WJ Branch, CP Naylor, and GT Macfarlane. Short chain fatty acids in human large intestine, portal, hepatic and venous blood. *Gut*, 28(10):1221–1227, 1987.
- [11] Gregory P Donaldson, S Melanie Lee, and Sarkis K Mazmanian. Gut biogeography of the bacterial microbiota. *Nature Reviews Microbiology*, 14(1):20–32, 2016.
- [12] Tamara El Bouti, Thierry Goudon, Simon Labarthe, Béatrice Laroche, Bastien Polizzi, Amira Rachah, Magali Ribot, and Rémi Tesson. A mixture model for the dynamic of the gut mucus layer. *ESAIM: Proceedings and Surveys*, 55:111–130, 2016.
- [13] Dirk Horstmann. Generalizing the keller–segel model: Lyapunov functionals, steady state analysis, and blow-up results for multi-species chemotaxis models in the presence of attraction and repulsion between competitive interacting species. *Journal of nonlinear science*, 21(2):231–270, 2011.
- [14] Institute of Medicine. *Dietary Reference Intakes for Water, Potassium, Sodium, Chloride, and Sulfate*. The National Academies Press, Washington, DC, 2005.
- [15] Malin EV Johansson, Jessica M Holmén Larsson, and Gunnar C Hansson. The two mucus layers of colon are organized by the muc2 mucin, whereas the outer layer is a legislator of host–microbial interactions. *Proceedings of the national academy of sciences*, 108(Supplement 1):4659–4665, 2011.

- [16] Malin EV Johansson, Henrik Sjövall, and Gunnar C Hansson. The gastrointestinal mucus system in health and disease. *Nature Reviews Gastroenterology and Hepatology*, 10(6):352–361, 2013.
- [17] Evelyn F Keller and Lee A Segel. Initiation of slime mold aggregation viewed as an instability. *Journal of Theoretical Biology*, 26(3):399–415, 1970.
- [18] MA Khashab, PJ Pickhardt, DH Kim, and DK Rex. Colorectal anatomy in adults at computed tomography colonography: normal distribution and the effect of age, sex, and body mass index. *Endoscopy*, 41(08):674–678, 2009.
- [19] Matieyendou Lamboni, Hervé Monod, and David Makowski. Multivariate sensitivity analysis to measure global contribution of input factors in dynamic models. *Reliability Engineering & System Safety*, 96(4):450–459, 2011.
- [20] Po Sing Leung. *The Gastrointestinal System: Gastrointestinal, Nutritional and Hepatobiliary Physiology*. Springer Science & Business, 2014.
- [21] Isabel Lozoya-Agullo, Isabel González-Álvarez, Marta González-Álvarez, Matilde Merino-Sanjuán, and Marival Bermejo. In situ perfusion model in rat colon for drug absorption studies: comparison with small intestine and caco-2 cell model. *Journal of pharmaceutical sciences*, 104(9):3136–3145, 2015.
- [22] M Minekus, M Smeets-Peeters, A Bernalier, S Marol-Bonnin, R Havenaar, P Marteau, M Alric, G Fonty, et al. A computer-controlled system to simulate conditions of the large intestine with peristaltic mixing, water absorption and absorption of fermentation products. *Applied microbiology and biotechnology*, 53(1):108–114, 1999.
- [23] Koen Molly, M Vande Woestyne, I De Smet, and Willy Verstraete. Validation of the simulator of the human intestinal microbial ecosystem (shime) reactor using microorganism-associated activities. *Microbial Ecology in Health and Disease*, 7(4):191–200, 1994.
- [24] Arun S Moorthy, Stephen PJ Brooks, Martin Kalmokoff, and Hermann J Eberl. A spatially continuous model of carbohydrate digestion and transport processes in the colon. *PloS one*, 10(12):e0145309, 2015.
- [25] R. Muñoz-Tamayo, B. Laroche, E. Walter, J. Doré, and M. Leclerc. Mathematical modelling of carbohydrate degradation by human colonic microbiota. *J. Theoret. Biol.*, 266(1):189–201, September 2010.
- [26] Jessica M. Oakes, Alison L. Marsden, Céline Grandmont, Shawn C. Shadden, Chantal Darquenne, and Irene Vignon-Clementel. Airflow and Particle Deposition Simulations in Health and Emphysema: From In Vivo to In Silico Animal Experiments. *Annals of Biomedical Engineering*, 42(4):899–914, April 2014.

- [27] Bastien Polizzi, Olivier Bernard, and Magali Ribot. A time-space model for the growth of microalgae biofilms for biofuel production. *Journal of theoretical biology*, 432:55–79, 2017.
- [28] L. Preziosi and A. Tosin. Multiphase modelling of tumour growth and extracellular matrix interaction: mathematical tools and applications. *J. Math. Biol.*, 58(4-5):625–656, 2009.
- [29] June L Round and Sarkis K Mazmanian. The gut microbiome shapes intestinal immune responses during health and disease. *Nature reviews. Immunology*, 9(5):313, 2009.
- [30] Inna Sekirov, Shannon L Russell, L Caetano M Antunes, and B Brett Finlay. Gut microbiota in health and disease. *Physiological reviews*, 90(3):859–904, 2010.
- [31] Ron Sender, Shai Fuchs, and Ron Milo. Revised estimates for the number of human and bacteria cells in the body. *PLoS biology*, 14(8):e1002533, 2016.
- [32] Felix Sommer and Fredrik Bäckhed. The gut microbiota—masters of host development and physiology. *Nature reviews. Microbiology*, 11(4):227, 2013.
- [33] Philip S Stewart. Diffusion in biofilms. *Journal of bacteriology*, 185(5):1485–1491, 2003.
- [34] David L Topping and Peter M Clifton. Short-chain fatty acids and human colonic function: roles of resistant starch and nonstarch polysaccharides. *Physiological reviews*, 81(3):1031–1064, 2001.
- [35] Pieter Van den Abbeele, Stefan Roos, Venessa Eeckhaut, Donald A MacKenzie, Melanie Derde, Willy Verstraete, Massimo Marzorati, Sam Possemiers, Barbara Vanhoecke, Filip Van Immerseel, et al. Incorporating a mucosal environment in a dynamic gut model results in a more representative colonization by lactobacilli. *Microbial biotechnology*, 5(1):106–115, 2012.
- [36] Nathan C Verberkmoes, Alison L Russell, Manesh Shah, Adam Godzik, Magnus Rosenquist, Jonas Halfvarson, Mark G Lefsrud, Juha Apajalahti, Curt Tysk, Robert L Hettich, et al. Shotgun metaproteomics of the human distal gut microbiota. *The ISME journal*, 3(2):179–189, 2009.
- [37] Jessica L Mark Welch, Yuko Hasegawa, Nathan P McNulty, Jeffrey I Gordon, and Gary G Borisy. Spatial organization of a model 15-member human gut microbiota established in gnotobiotic mice. *Proceedings of the National Academy of Sciences*, page 201711596, 2017.
- [38] Dietrich Winne and Walter Verheyen. Diffusion coefficient in native mucus gel of rat small intestine. *Journal of Pharmacy and Pharmacology*, 42(7):517–519, 1990.

A Model parameters and equations

A.1 Metabolic activity

We present in Fig. A.1 the graph of the metabolic capabilities of the microbial populations. The chemical reactions are represented with plain thick arrows and the volume transfers by dashed arrows. The thin dark arrows represent regulation processes such as inhibition or promotion. Complementary information can be found in the Petersen matrix of the processes (Tables A.1-A.5) or in the whole set of equations (Section A.2). In Tables A.1 and A.5, Y_{j,P_i} denotes the stoichiometric coefficient related to component $j \in I_C \cup I_S$ in process P_i .

We recall that $P_c \in \mathbb{R}^{8 \times 13}$ and $P_s \in \mathbb{R}^{8 \times 13}$ presented in Table A.1 are the reaction matrices for the mixture components and the solutes that store the yield of each process on the corresponding compounds, based on stoichiometry [25]. The kinetic rate vector $K = (K_p)_{p=P1, \dots, P13}$, the components of which are defined by $k_p \varphi_p$ for the different processes $p = P1, \dots, P13$ under consideration, are also recapitulated in Table A.1. For each process, k_p represents a unitary maximal kinetic rate whereas φ_p models saturation effects. Namely, φ_p is a Monod-like function for each metabolic process, except for the fibre and mucus hydrolysis, that is modeled with a Comtois law, according to [25] (see Table A.1).

A.2 Model equations and parameters

All the unknowns are summarized in Table A.2 and we can write the full set of equations for the model :

Mass balance equations for the mixture components :

	P1	P2	P3	P4	P5	P6	...
l	1	1	$-Y_{B_{mon},P3}$	$-Y_{B_{la},P4}$	$-Y_{B_{H_2a},P5}$	$-Y_{B_{H_2m},P6}$...
m	-1						...
pol		-1					...
B_{mon}			$Y_{B_{mon},P3}$...
B_{la}				$Y_{B_{la},P4}$...
B_{H_2a}					$Y_{B_{H_2a},P5}$...
B_{H_2m}						$Y_{B_{H_2m},P6}$...
r							...
mon	$Y_{mon,P1}$	$Y_{mon,P2}$	-1				...
la			$Y_{la,P3}$	-1			...
ac			$Y_{ac,P3}$	$Y_{ac,P4}$	$Y_{ac,P5}$...
pro			$Y_{pro,P3}$	$Y_{pro,P4}$...
but			$Y_{but,P3}$	$Y_{but,P4}$...
CH_4						$Y_{CH_4,P6}$...
CO_2			$Y_{CO_2,P3}$	$Y_{CO_2,P4}$	$Y_{CO_2,P5}$	$Y_{CO_2,P6}$...
H_2			$Y_{H_2,P3}$	$Y_{H_2,P4}$	-1	-1	...

	P7	P8	P9	P10	P11	P12	P13	
...	1	1	1	1				l
...								m
...								pol
...	-1							B_{mon}
...		-1						B_{la}
...			-1					$B_{H_2,a}$
...				-1				$B_{H_2,m}$
...								r
...								mon
...								la
...								ac
...								pro
...								but
...					-1			CH_4
...						-1		CO_2
...							-1	H_2

(a) Reaction matrix P_c (white background) and P_s (grey background).

	P1	P2	P3	P4	P5
φ_p	$\frac{f_m \cdot f_{B_{mon}}}{K_{x,P1} f_{B_{mon}} + f_m}$	$\frac{f_{pol} \cdot f_{B_{mon}}}{K_{x,P2} f_{B_{mon}} + f_{pol}}$	$\frac{c_{mon} \cdot f_{B_{mon}}}{f_l K_{s,P3} + c_{mon}}$	$\frac{c_{la} \cdot f_{B_{la}}}{f_l K_{s,P4} + c_{la}}$	$\frac{c_{H_2} \cdot f_{B_{H_2a}}}{f_l K_{s,P5} + c_{H_2}}$
k_p	k_{P1}	k_{P2}	k_{P3}	k_{P4}	k_{P5}
	P6	P7	P8	P9	P10
φ_p	$\frac{c_{H_2} \cdot f_{B_{H_2m}} \cdot I_{pH}}{f_l K_{s,P6} + c_{H_2}}$	$f_{B_{mon}}$	$f_{B_{la}}$	$f_{B_{H_2a}}$	$f_{B_{H_2m}}$
k_p	k_{P6}	k_{P7}	k_{P8}	k_{P9}	k_{P10}
	P11	P12	P13		
φ_p	$c_{CH_4} - K_{h,P11} RT [CH_{4,g}]_\infty$		$c_{CO_2} - K_{h,P12} RT [CO_{2,g}]_\infty$		$c_{H_2} - K_{h,P13} RT [H_{2,g}]_\infty$
k_p	k_{P11}		k_{P12}		k_{P13}

(b) Vector of the kinetic rates. For $p = P1, \dots, P13$, we have $K_p = k_p \rho_p$.

Table A.1: Petersen matrices and kinetic rate vectors.

Unknowns - volume fractions of mixture components			
Unknown	Unit	Description	Equation
f_m	[-]	Volume fraction of mucus	(1)
f_{pol}	[-]	Volume fraction of polysaccharides	(1)
f_l	[-]	Volume fraction of liquid	(1)
f_r	[-]	Volume fraction of digestible residuals	(1)
$f_{B_{mon}}$	[-]	Volume fraction of bacteria metabolizing monosaccharides	(1)
$f_{B_{la}}$	[-]	Volume fraction of bacteria metabolizing lactate	(1)
$f_{B_{H_2a}}$	[-]	Volume fraction of bacteria producing acetate from H_2	(1)
$f_{B_{H_2m}}$	[-]	Volume fraction of bacteria producing methane from H_2	(1)
Unknowns - diffusing compounds concentrations			
Unknown	Unit	Description	Equation
c_{mon}	mol.cm ⁻³	Concentration of monosaccharides	(5)
c_{la}	mol.cm ⁻³	Concentration of lactate	(5)
c_{H_2}	mol.cm ⁻³	Concentration of dissolved di-hydrogen	(5)
c_{ac}	mol.cm ⁻³	Concentration of acetate	(5)
c_{pro}	mol.cm ⁻³	Concentration of propionate	(5)
c_{bu}	mol.cm ⁻³	Concentration of butyrate	(5)
c_{CH_4}	mol.cm ⁻³	Concentration of methane	(5)
c_{CO_2}	mol.cm ⁻³	Concentration of dissolved carbone dioxyde	(5)
Unknowns - velocities			
u	cm.d ⁻¹	Average mixture velocity	(6)
\bar{u}	cm.d ⁻¹	Average velocity for the dissolved constituents	(4)
u_m	cm.d ⁻¹	Velocity field for mucus	(6)
u_{pol}	cm.d ⁻¹	Velocity field for polysaccharides	(6)
u_l	cm.d ⁻¹	Velocity field for liquid	(6)
u_r	cm.d ⁻¹	Velocity field for digestible residuals	(6)
$u_{B_{mon}}$	cm.d ⁻¹	Velocity field for bacteria B_{mon} (with chemotaxis)	(6)
$u_{B_{la}}$	cm.d ⁻¹	Velocity field for bacteria B_{la} (with chemotaxis)	(6)
$u_{B_{H_2a}}$	cm.d ⁻¹	Velocity field for bacteria B_{H_2a} (with chemotaxis)	(6)
$u_{B_{H_2m}}$	cm.d ⁻¹	Velocity field for bacteria B_{H_2m} (with chemotaxis)	(6)
$\vartheta_{B_{mon},chem}$	cm.d ⁻¹	Chemotactic velocity field for bacteria B_{mon}	(7)
$\vartheta_{B_{la},chem}$	cm.d ⁻¹	Chemotactic velocity field for bacteria B_{la}	(7)
$\vartheta_{B_{H_2a},chem}$	cm.d ⁻¹	Chemotactic velocity field for bacteria B_{H_2a}	(7)
$\vartheta_{B_{H_2m},chem}$	cm.d ⁻¹	Chemotactic velocity field for bacteria B_{H_2m}	(7)
Unknowns - chemotactic potential			
Φ_m	cm ²	Chemotactic potential produced by mucus	(8)
Φ_{pol}	cm ²	Chemotactic potential produced by polysaccharides	(8)
Φ_{mon}	mol.cm ⁻¹	Chemotactic potential produced by monosaccharides	(9)
Φ_{la}	mol.cm ⁻¹	Chemotactic potential produced by lactate	(9)
Φ_{H_2}	mol.cm ⁻¹	Chemotactic potential produced by di-hydrogen	(9)
Unknowns - pressure and viscosity			
p	g.cm ⁻¹ .d ⁻²	Pressure of the mixture	(12)
μ	g.cm ⁻¹ .d ⁻¹	Mixture viscosity	(13)
μ_m	g.cm ⁻¹ .d ⁻¹	Description of the mucus rheology	(14)
μ_l	g.cm ⁻¹ .d ⁻¹	Description of the liquid rheology	(15)
Unknowns - source functions			
F_i	d ⁻¹	Source function for the component $i \in I_C$	(1) - (18)
G_j	d ⁻¹	Source function for the component $j \in I_S$	(5) - (18)
K	d ⁻¹	Kinetic rate vector	(18)
ρ_p	[-]	Function modeling saturation effects for process p	-
Unknowns - boundary conditions			
γ_{f_i}	cm.d ⁻¹	Boundary flux for component $i \in I_C$	(16)
γ_{c_j}	mol.cm ⁻² .d ⁻¹	Boundary flux for component $j \in I_S$	(16)

Table A.2: Table of the unknowns of the model

$$\begin{aligned}
\partial_t f_m - \operatorname{div}(\sigma \nabla f_m) + \operatorname{div}(f_m u) &= -k_{P1} \frac{f_m \cdot f_{B_{mon}}}{K_{x,P1} f_{B_{mon}} + f_m} \\
\partial_t f_{pol} - \operatorname{div}(\sigma \nabla f_{pol}) + \operatorname{div}(f_{pol} u) &= -k_{P2} \frac{f_{pol} \cdot f_{B_{mon}}}{K_{x,P2} f_{B_{mon}} + f_{pol}} \\
\partial_t f_{B_{mon}} - \operatorname{div}(\sigma \nabla f_{B_{mon}}) + \operatorname{div}(f_{B_{mon}} u_{B_{mon}}) &= k_{P3} Y_{B_{mon},P3} f_l \frac{c_{mon} \cdot f_{B_{mon}}}{K_{s,P3} + c_{mon}} - k_{P7} f_{B_{mon}} \\
\partial_t f_{B_{la}} - \operatorname{div}(\sigma \nabla f_{B_{la}}) + \operatorname{div}(f_{B_{la}} u_{B_{la}}) &= k_{P4} Y_{B_{la},P4} f_l \frac{c_{la} \cdot f_{B_{la}}}{K_{s,P4} + c_{la}} - k_{P8} f_{B_{la}} \\
\partial_t f_{B_{H_2a}} - \operatorname{div}(\sigma \nabla f_{B_{H_2a}}) + \operatorname{div}(f_{B_{H_2a}} u_{B_{H_2a}}) &= k_{P5} Y_{B_{H_2a},P5} f_l \frac{c_{H_2} \cdot f_{B_{H_2a}}}{K_{s,P5} + c_{H_2}} - k_{P9} f_{B_{H_2a}} \\
\partial_t f_{B_{H_2m}} - \operatorname{div}(\sigma \nabla f_{B_{H_2m}}) + \operatorname{div}(f_{B_{H_2m}} u_{B_{H_2m}}) &= k_{P6} Y_{B_{H_2m},P6} f_l \frac{c_{H_2} \cdot f_{B_{H_2m}}}{K_{s,P6} + c_{H_2}} I_{pH} - k_{P10} f_{B_{H_2m}} \\
\partial_t f_r - \operatorname{div}(\sigma \nabla f_r) + \operatorname{div}(f_r u) &= 0 \\
\partial_t f_l - \operatorname{div}(\sigma \nabla f_l) + \operatorname{div}(f_l u) &= k_{P1} \frac{f_m \cdot f_{B_{mon}}}{K_{x,P1} f_{B_{mon}} + f_m} + k_{P2} \frac{f_{pol} \cdot f_{B_{mon}}}{K_{x,P2} f_{B_{mon}} + f_{pol}} \\
&\quad - k_{P3} Y_{B_{mon},P3} f_l \frac{c_{mon} \cdot f_{B_{mon}}}{K_{s,P3} + c_{mon}} - k_{P4} Y_{B_{la},P4} f_l \frac{c_{la} \cdot f_{B_{la}}}{K_{s,P4} + c_{la}} - k_{P5} Y_{B_{H_2a},P5} f_l \frac{c_{H_2} \cdot f_{B_{H_2a}}}{K_{s,P5} + c_{H_2}} \\
&\quad - k_{P6} Y_{B_{H_2m},P6} f_l \frac{c_{H_2} \cdot f_{B_{H_2m}}}{K_{s,P6} + c_{H_2}} I_{pH} + k_{P7} f_{B_{mon}} + k_{P8} f_{B_{la}} + k_{P9} f_{B_{H_2a}} + k_{P10} f_{B_{H_2m}} \\
\text{where } I_{pH}(z) &:= \exp \left(-3 \left(\frac{pH(z) - I_{pH,high}}{I_{pH,high} - I_{pH,low}} \right)^2 \right) \mathbf{1}_{pH(z) < I_{pH,high}} + \mathbf{1}_{pH(z) \geq I_{pH,high}} \\
\text{and } pH(z) &= I_{pH,min} + (I_{pH,max} - I_{pH,min})z/L
\end{aligned}$$

Volume constraint :

$$\sum_{i \in I_C} f_i(t, x) = 1$$

Mass balance equations for the dissolved compounds :

$$\begin{aligned}
\partial_t c_{mon} - \text{div}(\sigma_{mon} \nabla c_{mon}) + \text{div}(c_{mon} \tilde{u}) &= k_{P1} Y_{mon,P1} \frac{f_m \cdot f_{B_{mon}}}{K_{x,P1} f_{B_{mon}} + f_m} \\
&+ k_{P2} Y_{mon,P2} \frac{f_{pol} \cdot f_{B_{mon}}}{K_{x,P2} f_{B_{mon}} + f_{pol}} - k_{P3} f_l \frac{c_{mon} \cdot f_{B_{mon}}}{K_{s,P3} + c_{mon}} \\
\partial_t c_{la} - \text{div}(\sigma_{la} \nabla c_{la}) + \text{div}(c_{la} \tilde{u}) &= k_{P3} Y_{la,P3} f_l \frac{c_{mon} \cdot f_{B_{mon}}}{K_{s,P3} + c_{mon}} - k_{P4} f_l \frac{c_{la} \cdot f_{B_{la}}}{K_{s,P4} + c_{la}} \\
\partial_t c_{ac} - \text{div}(\sigma_{ac} \nabla c_{ac}) + \text{div}(c_{ac} \tilde{u}) &= k_{P3} Y_{ac,P3} f_l \frac{c_{mon} \cdot f_{B_{mon}}}{K_{s,P3} + c_{mon}} + k_{P4} Y_{ac,P4} f_l \frac{c_{la} \cdot f_{B_{la}}}{K_{s,P4} + c_{la}} \\
&+ k_{P5} Y_{ac,P5} f_l \frac{c_{H_2} \cdot f_{B_{H_2a}}}{K_{s,P5} + c_{H_2}} \\
\partial_t c_{pro} - \text{div}(\sigma_{pro} \nabla c_{pro}) + \text{div}(c_{pro} \tilde{u}) &= k_{P3} Y_{pro,P3} f_l \frac{c_{mon} \cdot f_{B_{mon}}}{K_{s,P3} + c_{mon}} + k_{P4} Y_{pro,P4} f_l \frac{c_{la} \cdot f_{B_{la}}}{K_{s,P4} + c_{la}} \\
\partial_t c_{but} - \text{div}(\sigma_{but} \nabla c_{but}) + \text{div}(c_{but} \tilde{u}) &= k_{P3} Y_{but,P3} f_l \frac{c_{mon} \cdot f_{B_{mon}}}{K_{s,P3} + c_{mon}} + k_{P4} Y_{but,P4} f_l \frac{c_{la} \cdot f_{B_{la}}}{K_{s,P4} + c_{la}} \\
\partial_t c_{CH_4} - \text{div}(\sigma_{CH_4} \nabla c_{CH_4}) + \text{div}(c_{CH_4} \tilde{u}) &= k_{P6} Y_{CH_4,P6} f_l \frac{c_{H_2} \cdot f_{B_{H_2m}}}{K_{s,P6} + c_{H_2}} I_{pH} \\
&- k_{P11} (c_{CH_4} - K_{h,P11} RT[CH_{4,g}]_{\infty}) \\
\partial_t c_{CO_2} - \text{div}(\sigma_{CO_2} \nabla c_{CO_2}) + \text{div}(c_{CO_2} \tilde{u}) &= k_{P3} Y_{CO_2,P3} f_l \frac{c_{mon} \cdot f_{B_{mon}}}{K_{s,P3} + c_{mon}} \\
&+ k_{P4} Y_{CO_2,P4} f_l \frac{c_{la} \cdot f_{B_{la}}}{K_{s,P4} + c_{la}} + k_{P5} Y_{CO_2,P5} f_l \frac{c_{H_2} \cdot f_{B_{H_2a}}}{K_{s,P5} + c_{H_2}} + k_{P6} Y_{CO_2,P6} f_l \frac{c_{H_2} \cdot f_{B_{H_2m}}}{K_{s,P6} + c_{H_2}} I_{pH} \\
&- k_{P12} (c_{CO_2} - K_{h,P12} RT[CO_{2,g}]_{\infty}) \\
\partial_t c_{H_2} - \text{div}(\sigma_{H_2} \nabla c_{H_2}) + \text{div}(c_{H_2} \tilde{u}) &= k_{P3} Y_{H_2,P3} f_l \frac{c_{mon} \cdot f_{B_{mon}}}{K_{s,P3} + c_{mon}} + k_{P4} Y_{H_2,P4} f_l \frac{c_{la} \cdot f_{B_{la}}}{K_{s,P4} + c_{la}} \\
&- k_{P5} f_l \frac{c_{H_2} \cdot f_{B_{H_2a}}}{K_{s,P5} + c_{H_2}} - k_{P6} f_l \frac{c_{H_2} \cdot f_{B_{H_2m}}}{K_{s,P6} + c_{H_2}} I_{pH} - k_{P13} (c_{H_2} - K_{h,P13} RT[H_{2,g}]_{\infty})
\end{aligned}$$

Stokes equation for the velocity field of the carrying fluid :

$$\begin{aligned}
\nabla p - \frac{1}{2} \text{div}(\mu(f_m, f_l)(\nabla u + \nabla u^T)) &= 0, \\
\text{with } \mu(f_m, f_l) &= \max_{k=m,l} \left(\mu_{k,min} + (\mu_{k,max} - \mu_{k,min}) \frac{f_k^{2\alpha_k}}{f_{k,thr}^{2\alpha_k} + f_k^{2\alpha_k}} \right)
\end{aligned}$$

Definition of the velocities :

$$u_i = u + \vartheta_{i,chem}, \text{ where } \vartheta_{i,chem} = \sum_j \lambda_{ij} \nabla \Phi_j, \text{ if } i \in I_B = \{B_{mon}, B_{la}, B_{H_2a}, B_{H_2m}\}$$

$$\tilde{u} = u + \sum_{i \in I_B} f_i \vartheta_{i,chem}$$

Poisson equations for the chemotactic potential :

$$\begin{aligned} -\Delta\Phi_j &= f_j - \frac{1}{|\omega|} \int_{\omega} f_j(x, z) dx \text{ in } \Omega, \quad \nabla\Phi_j \cdot \eta = 0 \text{ on } \partial\Omega, \quad \text{when } j \in \{m, pol\} \\ -\Delta\Phi_j &= c_j - \frac{1}{|\omega|} \int_{\omega} c_j(x, z) dx \text{ in } \Omega, \quad \nabla\Phi_j \cdot \eta = 0 \text{ on } \partial\Omega, \quad \text{when } j \in \{mon, la, H_2\} \end{aligned}$$

Boundary conditions :

On Γ_{in} :

$$\begin{aligned} u \cdot \eta &= U_{in} = V_{in}/|\omega| \\ (-\sigma\nabla f_i + f_i u) \cdot \eta &= U_{in} f_{i,in}, \text{ when } i \in I_C \\ (-\sigma_j \nabla c_j + c_j u) \cdot \eta &= \begin{cases} U_{in} c_{j,in}, & \text{when } j = mon \\ 0, & \text{when } j \in I_S \setminus \{mon\} \end{cases} \end{aligned}$$

On Γ_m :

$$\begin{aligned} (-\sigma\nabla f_m + f_m u) \cdot \eta &= g_m(f_m - f_m^*) \\ (-\sigma\nabla f_l + f_l u) \cdot \eta &= \begin{cases} g_{l,max} f_l \text{ for } z \in [0, L_{pump}^{max}], \\ \left(g_{l,max} - \frac{z-L_{prox}}{L_{trans}} (g_{l,max} - g_{l,min}) \right) f_l \text{ for } z \in [L_{pump}^{max}, L_{pump}^{min}], \\ g_{l,min} f_l \text{ for } z \in [L_{pump}^{min}, L] \end{cases} \\ (-\sigma\nabla f_i + f_i u) \cdot \eta &= 0, \text{ when } i \in I_C \setminus \{l, m\} = \{pol, r, B_{mon}, B_{la}, B_{H_2a}, B_{H_2m}\} \\ (-\sigma_j \nabla c_j + c_j u) \cdot \eta &= g_{j,max} - (g_{j,max} - g_{j,min}) \frac{z}{L} \text{ for } j \in \{la, ac, pro, bu\}, \\ (-\sigma_j \nabla c_j + c_j u) \cdot \eta &= 0 \text{ when } j \in \{mon, H_2, CH_4, CO_2\}, \\ u_i \cdot \eta &= \sum_{i \in I_C} \gamma_{f_i} + U_{per,r}, \quad u_i \cdot \eta_z = U_{per,z}. \end{aligned}$$

On Γ_{out} :

$$\begin{aligned} (-\sigma\nabla f_i + f_i u) \cdot \eta &= f_i u_i \cdot \eta, \text{ when } i \in I_C \\ (-\sigma_j \nabla c_j + c_j u) \cdot \eta &= c_j u \cdot \eta, \text{ when } j \in I_S \end{aligned}$$

We recall that those previous equations are not directly solved numerically. Instead, we solve their asymptotic approximations (20)-(21) with the speed approximations (24)-(25) and the approximations of the chemotactic potentials (22)-(23).

B Supplementary materials

Model unknowns of the asymptotic model: mixture components			
Unknown	Unit	Description	Equation
f_m	[-]	Mucus volume fraction approximation	(20)
f_{pol}	[-]	Polysaccharide volume fraction approximation	(20)
$f_{B_{mon}}$	[-]	Approx. of the volume fraction of B_{mon}	(20)
$f_{B_{la}}$	[-]	Approx. of the volume fraction of B_{la}	(20)
$f_{B_{H_2a}}$	[-]	Approx. of the volume fraction of B_{H_2a}	(20)
$f_{B_{H_2m}}$	[-]	Approx. of the volume fraction of B_{H_2m}	(20)
f_l	[-]	Liquid chyme volume fraction approximation	(20)
f_r	[-]	Undigestible residual volume fraction approximation	(20)
Model unknowns of the asymptotic model: diffusing compounds			
Unknown	Unit	Description	Equation
c_{mon}	mol.cm ⁻³	Diffusing monosaccharides approximation	(21)
c_{lac}	mol.cm ⁻³	Diffusing lactate approximation	(21)
c_{H_2}	mol.cm ⁻³	Diffusing hydrogen approximation	(21)
c_{ac}	mol.cm ⁻³	Diffusing acetate approximation	(21)
c_{pro}	mol.cm ⁻³	Diffusing propionate approximation	(21)
c_{bu}	mol.cm ⁻³	Diffusing butyrate approximation	(21)
c_{CH_4}	mol.cm ⁻³	Diffusing methane approximation	(21)
c_{CO_2}	mol.cm ⁻³	Diffusing carbon dioxide approximation	(21)
Model unknowns: speed approximations			
Unknown	Unit	Description	Equation
u_r	cm.day ⁻¹	Average mixture speed approximation	(24)-(25)
\tilde{u}	cm.day ⁻¹	Average speed for diffusing solutes approximation	(4)
$\vartheta_{B_{mon},r}$	cm.day ⁻¹	Chemotactic speed for the $f_{B_{mon}}$ phase approx.	(22)
$\vartheta_{B_{la},r}$	cm.day ⁻¹	Chemotactic speed for the $f_{B_{la}}$ phase approx.	(22)
$\vartheta_{B_{H_2a},r}$	cm.day ⁻¹	Chemotactic speed for the $f_{B_{H_2a}}$ phase approx.	(22)
$\vartheta_{B_{H_2m},r}$	cm.day ⁻¹	Chemotactic speed for the $f_{B_{H_2m}}$ phase approx.	(22)
Chemotactic potential approximations			
Unknown	Unit	Description	Equation
Υ_m	cm ²	Chemotactic potential towards mucus approx.	(23)
Υ_{pol}	cm ²	Chemotactic potential towards polysaccharides approx.	(23)
Υ_{mon}	mol.cm ⁻¹	Chemotactic potential towards monosaccharides approx.	(23)
Υ_{la}	mol.cm ⁻¹	Chemotactic potential towards lactate approx.	(23)
Υ_{H_2}	mol.cm ⁻¹	Chemotactic potential towards H_2 approx.	(23)

Table A.3: **Asymptotic model unknowns.** The unknowns of the asymptotic model are listed with their units. The asymptotic model is numerically solved, giving an accurate approximation of the original model, with a small computational load.

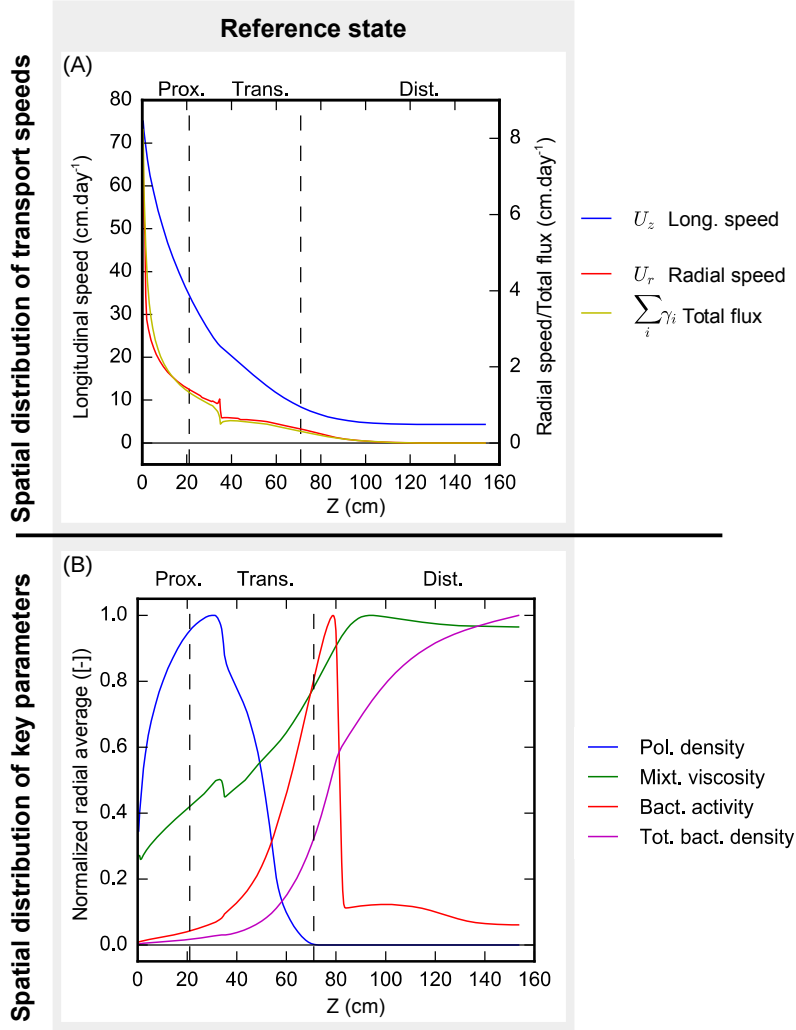


Figure 2: **Transport speeds and key parameters of the spatial structure.** (A, top) The longitudinal distribution of the radially averaged radial ($U_r(z) := \frac{2}{R^2} \int_0^R r u_{s,r}(r, z) dr$) and longitudinal speeds ($U_z(z) := \frac{2}{R^2} \int_0^R r u_{s,z}(r, z) dr$), together with the total flux of water and mucus through the mucosa ($\sum_i \gamma_i$), are displayed. We indicate by vertical dashed lines the limits of the colon compartments that are considered for observation issues: proximal, transverse and distal colons. (B, bottom) The averaged values of key parameters along the colon are presented. The different quantities are normalized by their maximal value to allow representation in the same graph. The maximal values of polysaccharide density, mixture viscosity, microbial functional activity and total microbial density are respectively $6.74e-2$, $3.88e3 \text{g cm}^{-1} \text{d}^{-1}$, $8.34e-3 \text{d}^{-1}$ and $6.10e-2$. The slope breaks that are observed at $z \simeq 35 \text{cm}$ on the red, yellow and green curves are modelling artefacts due to the different water pumping activities applied distally and proximally in the model (cf the boundary condition definitions in Sec. 2.1.8): this slope rupture is located at the junction between both zones.

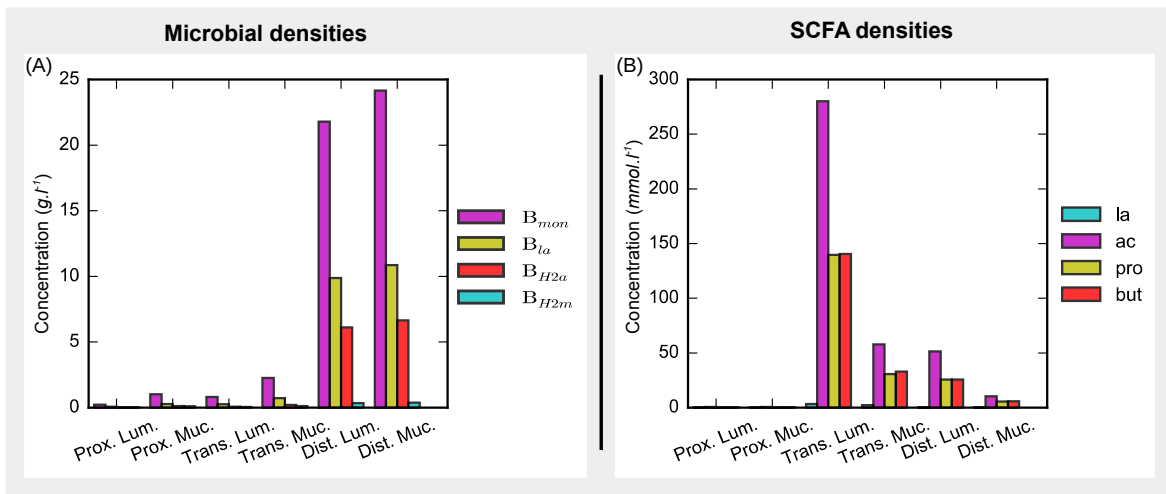


Figure 3: **Microbial and SCFA levels in the different compartments.** We display bar plots of the microbial populations (A) and SCFA (B) averaged densities in 6 different compartments of the large intestine, formed by the luminal and mucosal regions in the proximal, transverse and distal colons. The mucosal area is defined by the points located at less than 0.2cm from the mucosal boundary.

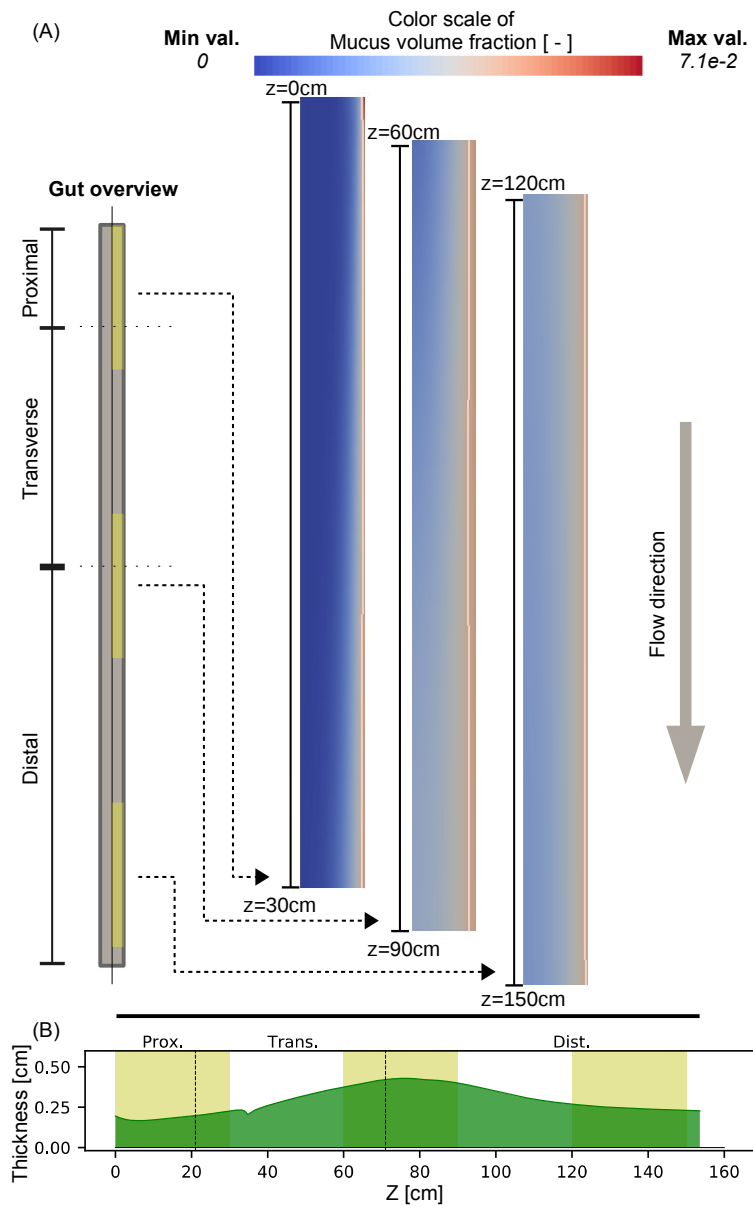


Figure 4: **Spatial distribution of the mucus in the colon.** The steady-state mucus distribution is displayed in the proximal, transverse and distal parts (A, top) of the large intestine together with the isoline $m = 0.0425$ which represents in our model the limit of the mucus layer: we represent longitudinal sections (for $r \geq 0$) of the cylindrical colon; the axis of the cylinder is the left boundary of the images while the right boundary is the mucosa; the upper part of the images is the most proximal and the digestive flux is directed from the top to the bottom of the figure. We then display the mucus layer thickness (B, bottom, green plot). The mucus layer is thin in the proximal colon and gets thicker in the transverse part, to be reduced again in the distal bowel. The yellow zones that are displayed in the schematic view of the colon and in the mucus layer plot indicate the domains covered by the proximal, transverse and distal plots of A.

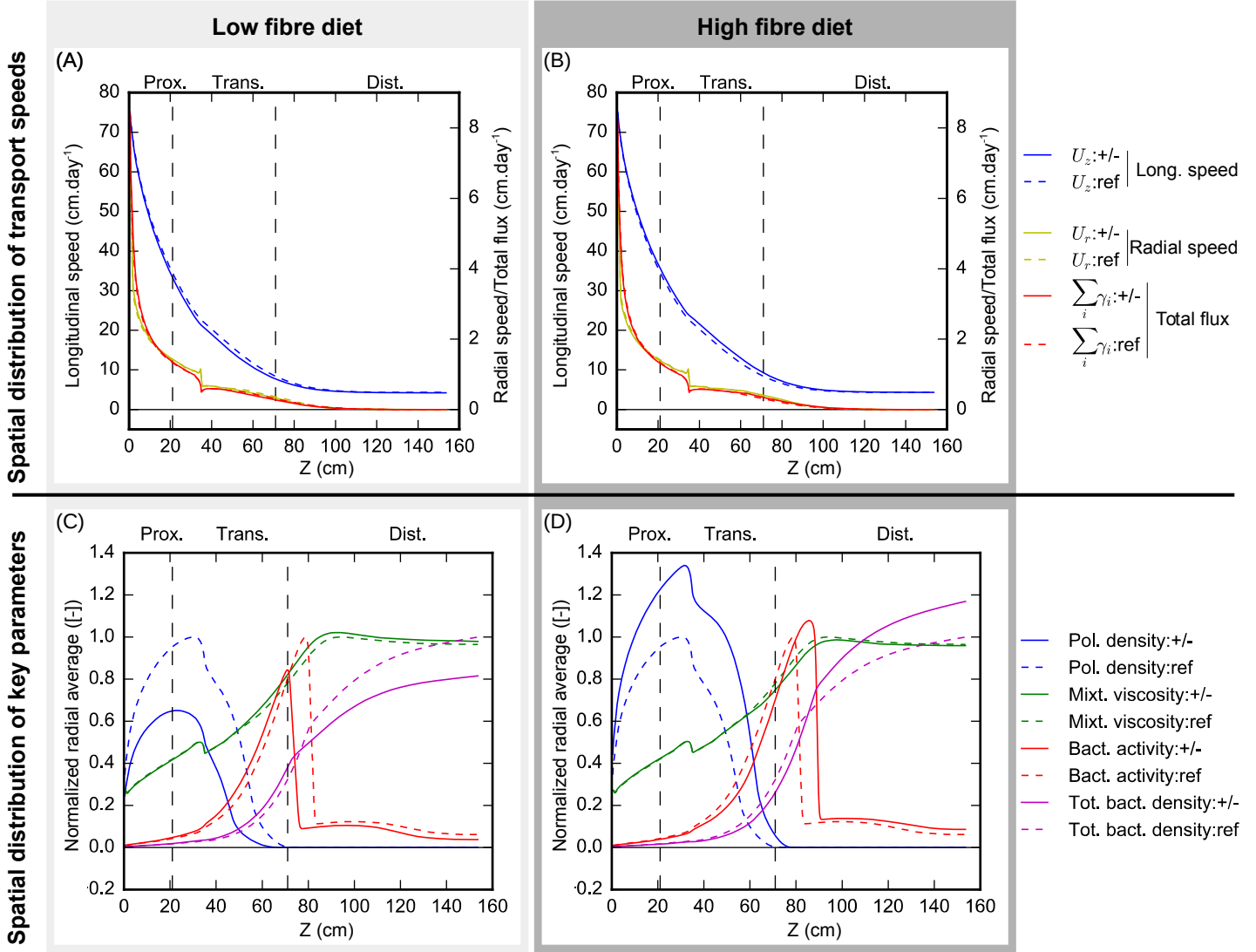


Figure 5: Impact of the diet on the transport speeds and on the spatial structure. We reproduce the quantities of Fig. 2, with a low-fibre diet (30% decrease of polysaccharide input, (A) and (C)) and high-fibre diet (30% increase, (B) and (D)), that we compare with the reference fibre diet (same polysaccharide input, dashed lines). In the upper panels (A) and (B), the speed distribution is reproduced, whereas the lower panels (C) and (D) display the spatial distribution of relevant parameters: all the values are normalized respectively to the maximal values of the reference diet (see Fig 2 for nominal values). Higher fibre diet enhances the transit speed, the fibre concentration, the bacterial activity and the microbial levels, while slightly locally reducing the viscosity. Less fibres diet leads to an opposite effect.

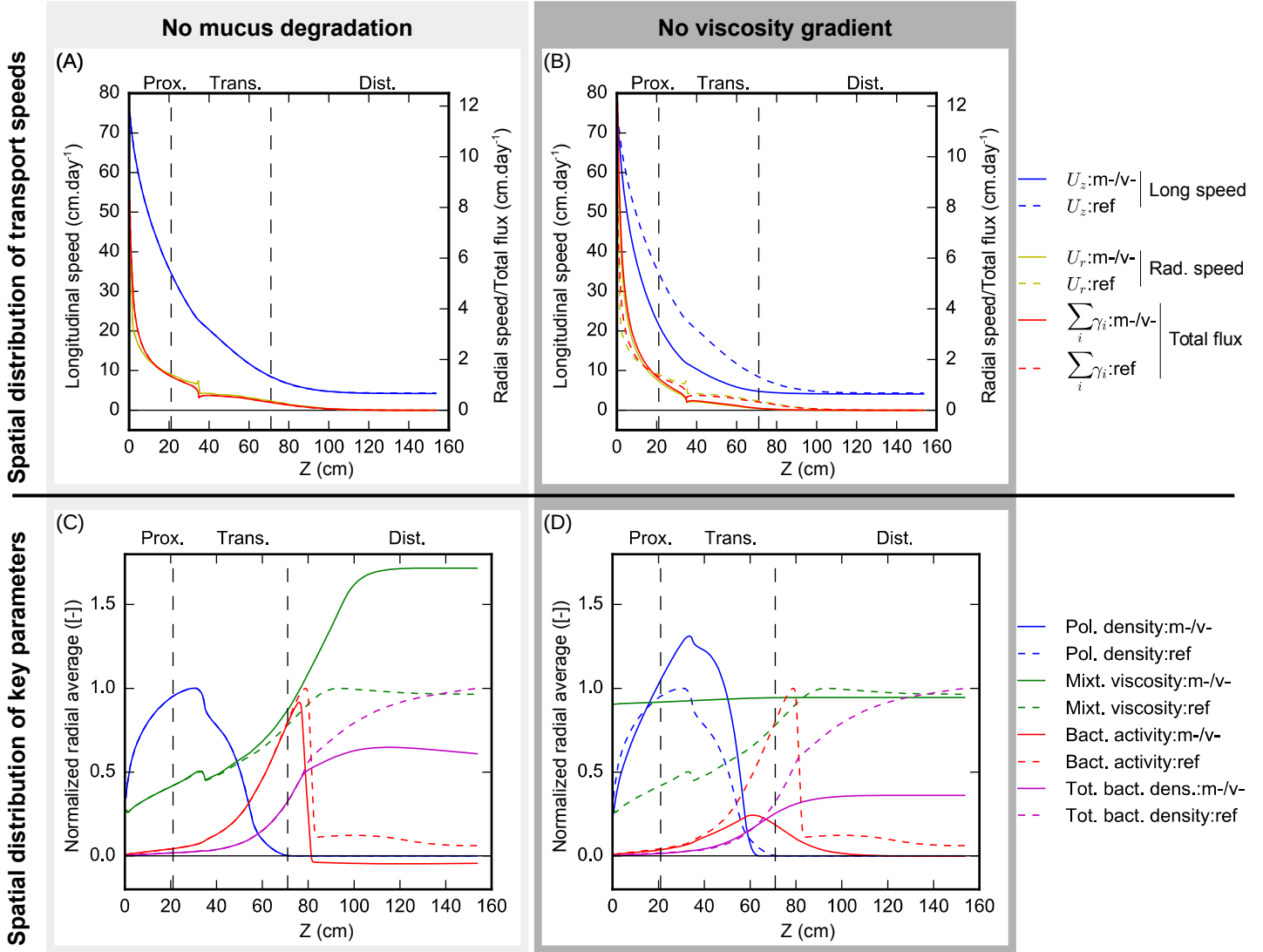


Figure 6: **Impact of viscosity and mucus degradation on the outcome of the model.** We reproduce the quantities of Fig. 2 with no mucus degradation ($m-$, A and C) or with a homogeneous viscosity ($v-$, B and D), compared with the reference-fibre diet of Fig. 2 (ref , dashed lines). All the values are normalized respectively to the maximal values of the reference. The mucus degradation has an effect in the distal bowel only. A homogeneous viscosity has a deep impact on the bacterial activity and the microbial levels.

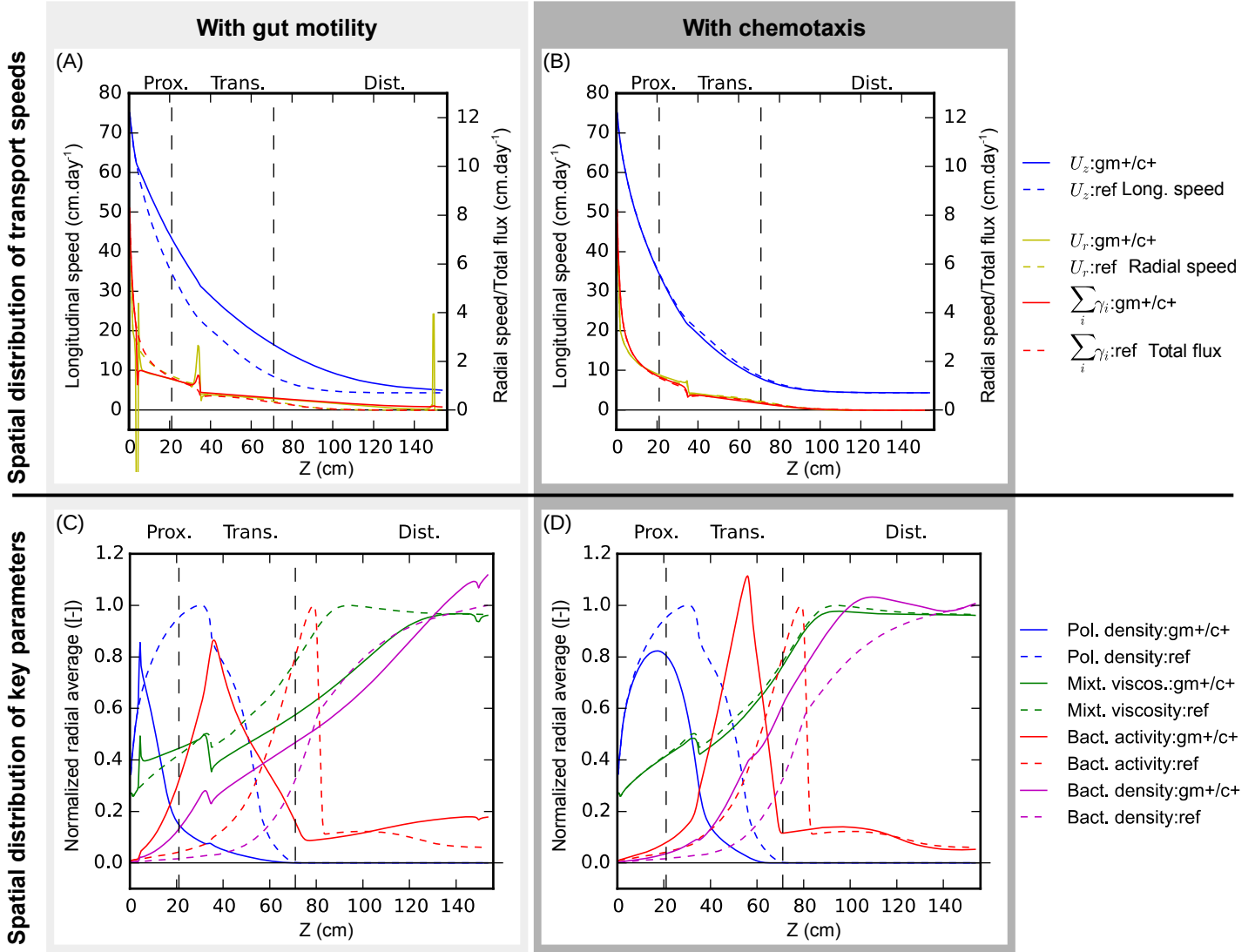


Figure 7: Impact of peristalsis and chemotaxis on the outcome of the model. We reproduce the quantities of Fig. 2 with epithelial motile activity ($gm+$, A and C) or chemotactic active swimming ($c+$, B and D), compared with the reference-fibre diet of Fig. 2 (ref , dashed lines). All the values are normalized respectively to the maximal values of the reference. The epithelial motility shifts proximally the bacterial activity, enhancing the bacterial levels in the proximal and transverse colon, while reducing the viscosity. The bacterial active motion promotes an earlier colonization of the colon, resulting in increasing proximally the metabolic activity and the microbial concentrations.

Spatial distribution of key parameters

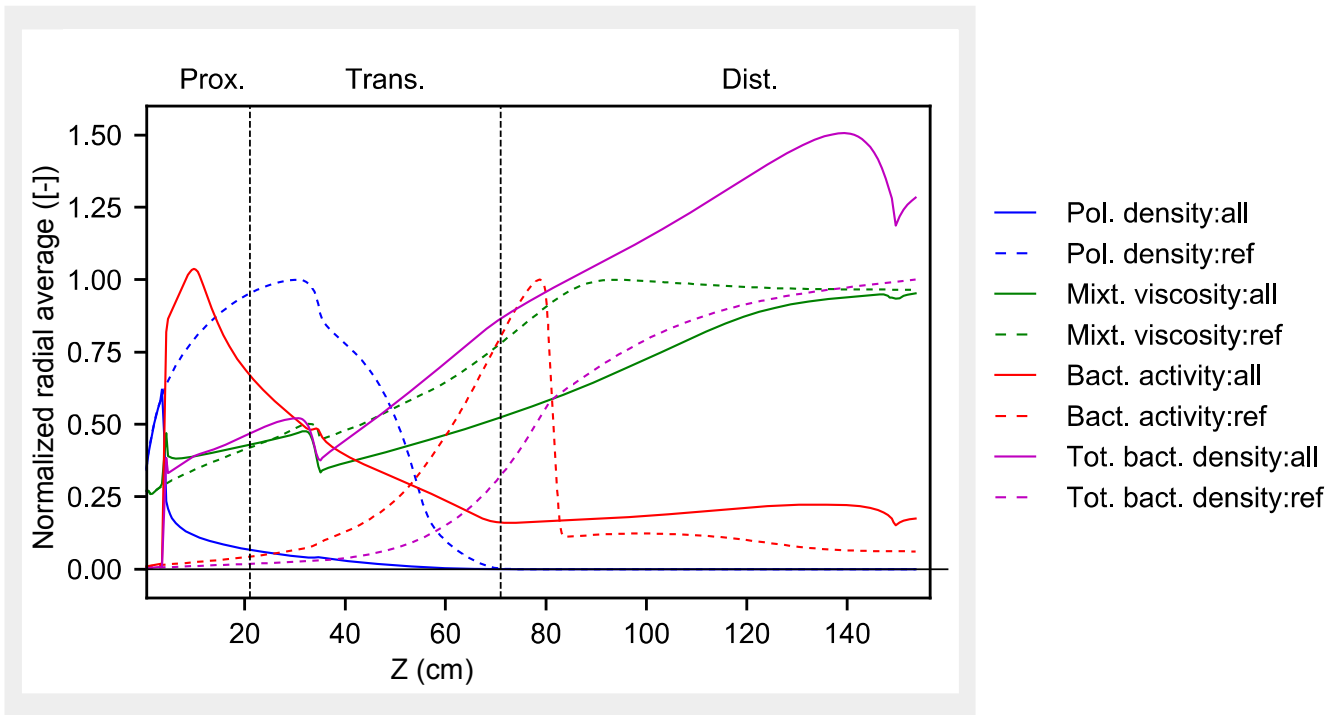


Figure 8: **Longitudinal distribution of the averaged key parameters when all the mechanisms are combined.** We investigate the impact of the combination of all the effects on the outcome of the model. We reproduce the quantities of Fig. 2 with all the mechanisms, i.e. peristalsis, viscosity gradients and chemotaxis (*all*, circle lines), compared with the reference-fibre diet of Fig. 2 (*ref*, dashed lines). All the values are normalized respectively to the maximal values of the reference. The metabolic activity and the bacterial levels are boosted when all the mechanisms are combined.

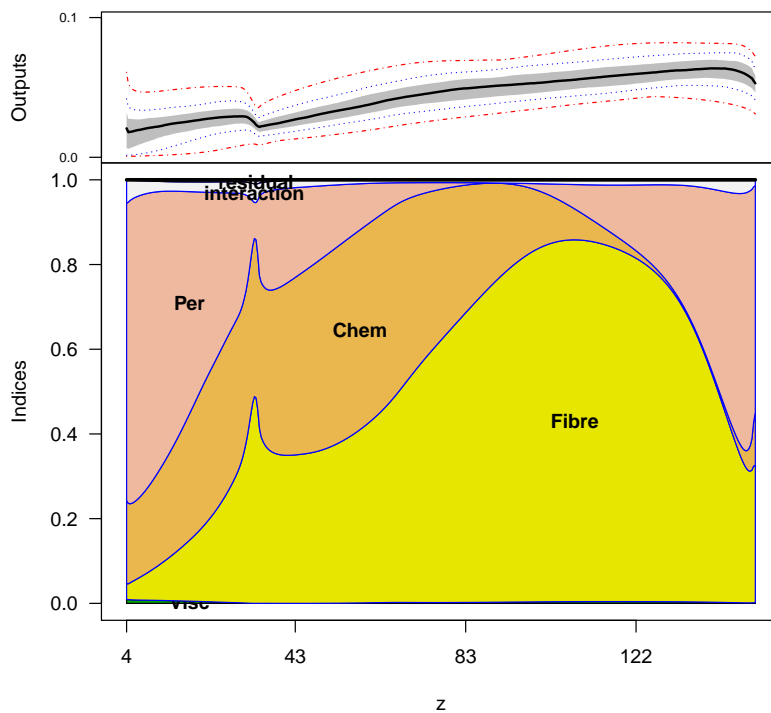


Figure 9: **Longitudinal distribution of the first order Sobol index.** We perform a global sensitivity analysis to assess the impact of the parameters driving the peristalsis, the fibre input, the mixture viscosity and the chemotaxis magnitude on the longitudinal distribution of the radially averaged bacterial populations (i.e. on $B(z) := \sum_{i \in I_B} \frac{2}{R^2} \int_0^R r c_i(z, r) dr$). For each z in $(0, L)$, the upper plot displays the dispersion of $B(z)$ when sampling the parameter space by indicating the extremal values (red dashed lines), the first and last deciles (blue dot lines), the second and third quartiles (gray zones) and the median value (black bold line). The lower panel displays for each z the first order Sobol index of each parameter, i.e. the part of the total output variance explained by a given parameter. Per: peristalsis magnitude, Fibre: level of fibre input, Chem: magnitude of the chemotactic activity, Visc: mixture viscosity. Interaction: second order Sobol Index. Residual: residual in the total variance decomposition. The epithelial motility is preponderant in the proximal part, while fibre levels is the main driver of the bacterial levels in the distal compartments. In the transverse colon, fibre intake and bacterial chemotaxis are the more important mechanisms. The spikes at $z \simeq 35$ cm are produced by modelling artefacts of the boundary condition on l (see fig. 2)

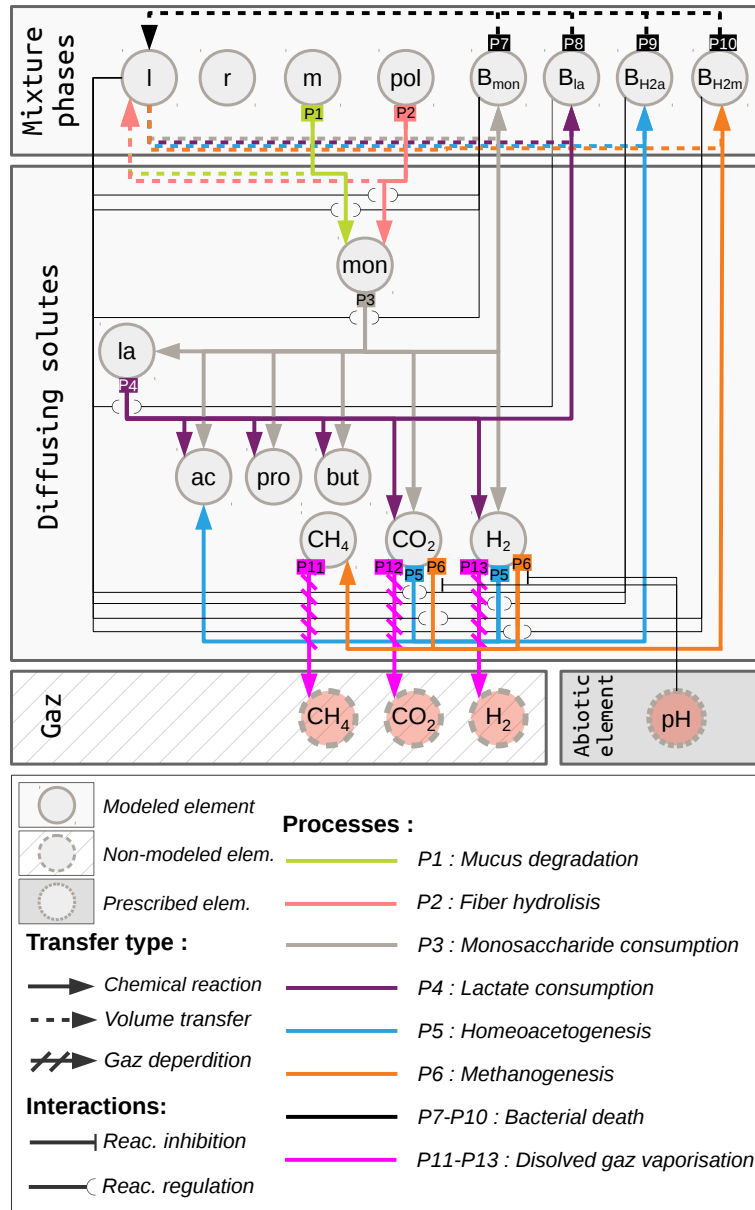


Figure A.1: **Graph of the reactions and volume transfers considered in the model.** We represent the functional interactions between the mixture components of I_C (liquid l , digestive residuals r , mucus m , polysaccharides pol , and the bacterial populations B_{mon} , B_{la} , B_{H2a} and B_{H2m}) and the diffusing solutes of I_S (monosaccharides mon , lactate la , acetate ac , propionate pro , butyrate but , methane CH_4 , carbone dioxide CO_2 and hydrogen H_2). We represent in the graph gaseous components, but they are not explicitly modeled: they represent sink sources for the corresponding diffusing solutes. A fixed pH gradient is prescribed on the domain: it interacts with the process P6.

Geometrical parameters				
Parameter	Value	Unit	Description	Ref.
L	154	cm	Total gut length	[25]
R	2.5	cm	Gut radius	[25]
L_{prox}	21	cm	Proximal colon length	[25]
L_{trans}	70	cm	Transverse colon length	[25]
L_{dist}	63	cm	Distal colon length	[25]
Diffusion parameters				
Parameter	Value	Unit	Description	Ref.
σ	0.8	$\text{cm}^2.\text{d}^{-1}$	Diffusion coefficient: mixture component	-
σ_{mon}	1.4	$\text{cm}^2.\text{d}^{-1}$	Diffusion coefficient: monosaccharides	-
σ_{la}	1.4	$\text{cm}^2.\text{d}^{-1}$	Diffusion coefficient: lactate	-
σ_{ac}	1.4	$\text{cm}^2.\text{d}^{-1}$	Diffusion coefficient: acetate	-
σ_{pro}	1.4	$\text{cm}^2.\text{d}^{-1}$	Diffusion coefficient: propionate	-
σ_{but}	1.4	$\text{cm}^2.\text{d}^{-1}$	Diffusion coefficient: butyrate	-
σ_{H_2}	0.8	$\text{cm}^2.\text{d}^{-1}$	Diffusion coefficient: H_2	-
σ_{CH_4}	2	$\text{cm}^2.\text{d}^{-1}$	Diffusion coefficient: CH_4	-
σ_{CO_2}	2	$\text{cm}^2.\text{d}^{-1}$	Diffusion coefficient: CO_2	-
Viscosity parameters				
Parameter	Value	Unit	Description	Ref.
$\mu_{l,min}$	$0.864 \cdot 10^3$	$\text{g.cm}^{-1}.\text{d}^{-1}$	Water viscosity	[5]
$\mu_{l,max}$	$36.7 \cdot 10^3$	$\text{g.cm}^{-1}.\text{d}^{-1}$	Viscosity of dried mixture.	-
$f_{l,thr}$	0.5	[-]	Viscosity threshold: liquid sigmoid	-
α_l	2	[-]	Stiffness: liquid sigmoid	-
$\mu_{m,min}$	$0.864 \cdot 10^3$	$\text{g.cm}^{-1}.\text{d}^{-1}$	Minimal mucus viscosity	[5]
$\mu_{m,max}$	$73.4 \cdot 10^3$	$\text{g.cm}^{-1}.\text{d}^{-1}$	Maximal mucus viscosity	[5]
$f_{m,thr}$	0.0425	[-]	Viscosity threshold: mucus sigmoid	-
α_m	7	[-]	Stiffness: mucus sigmoid	-
Chemotactic parameters				
Parameter	Value	Unit	Description	Ref.
$\lambda_{B_{mon},m}$	82.64	d^{-1}	Mucus chemotactic coefficient for B_{mon}	-
$\lambda_{B_{mon},pol}$	28.32	d^{-1}	Polysaccharides coefficient for B_{mon}	-
$\lambda_{B_{mon},mon}$	$9.32 \cdot 10^3$	$\text{cm}^3.\text{mol}^{-1}.\text{d}^{-1}$	Monosaccharides coefficient for B_{mon}	-
$\lambda_{B_{la},la}$	$0.85 \cdot 10^7$	$\text{cm}^3.\text{mol}^{-1}.\text{d}^{-1}$	Lactate chemotactic coefficient for B_{la}	-
$\lambda_{B_{H_2a},H_2}$	$0.68 \cdot 10^7$	$\text{cm}^3.\text{mol}^{-1}.\text{d}^{-1}$	H_2 chemotactic coefficient for B_{H_2a}	-
$\lambda_{B_{H_2m},H_2}$	$0.68 \cdot 10^7$	$\text{cm}^3.\text{mol}^{-1}.\text{d}^{-1}$	H_2 chemotactic coefficient for B_{H_2m}	-
Initial condition				
Parameter	Value	Unit	Description	Ref.
$f_{m,min}^{init}$	0	[-]	No mucus in lumen	[25]
$f_{m,max}^{init}$	0.05	[-]	Maximal quantity of mucins	[25]
r_m	2.25	cm	Threshold: initial condition	-
α_m^{init}	4	[-]	Stiffness: initial condition	-
Other parameters and units				
Parameter	Value	Unit	Description	Ref.
ρ	1	g.cm^{-1}	Mass density	-

Table A.4: **Geometrical, diffusion, viscosity and initial condition parameters.** The diffusion coefficients are calculated from order of magnitude of reported diffusion coefficients of the different compounds in water [33] multiplied by the corresponding diffusive ratio between water and mucus as reported in [38]. The viscosity of the dried mixture was set to half the mucus viscosity.

Source Function				
Parameter	Value	Unit	Description	Ref.
α	0.113	$\text{cm}^3 \cdot \text{mol}^{-1}$	Multiplicative constant for unit conversion	
k_{P1}	1.20e3	d^{-1}	Maximum specific reaction rate for P1	[25]
k_{P2}	1.20e3	d^{-1}	Maximum specific reaction rate for P2	[25]
k_{P3}	7.92	d^{-1}	Maximum specific reaction rate for P3	[25]
k_{P4}	103	d^{-1}	Maximum specific reaction rate for P4	[25]
k_{P5}	108.837	d^{-1}	Maximum specific reaction rate for P5	[25]
k_{P6}	22.581	d^{-1}	Maximum specific reaction rate for P6	[25]
k_{P7}	0.01	d^{-1}	Maximum specific reaction rate for P7	[25]
k_{P8}	0.01	d^{-1}	Maximum specific reaction rate for P8	[25]
k_{P9}	0.01	d^{-1}	Maximum specific reaction rate for P9	[25]
k_{P10}	0.01	d^{-1}	Maximum specific reaction rate for P10	[25]
k_{P11}	200	d^{-1}	Maximum specific reaction rate for P11	[25]
k_{P12}	200	d^{-1}	Maximum specific reaction rate for P12	[25]
k_{P13}	200	d^{-1}	Maximum specific reaction rate for P13	[25]
$K_{h,P11}$	0.0011	$\text{mol} \cdot \text{bar}^{-1}$	Henry's Law coefficient	[25]
$K_{h,P12}$	0.0255	$\text{mol} \cdot \text{bar}^{-1}$	Henry's Law coefficient	[25]
$K_{h,P13}$	7.29e-4	$\text{mol} \cdot \text{bar}^{-1}$	Henry's Law coefficient	[25]
R	0.08314	$\text{bar} \cdot \text{mol}^{-1} \cdot \text{K}^{-1}$	Ideal gas constant	[25]
T	310.15	K	Gut absolute temperature	[25]
$[CH_{4,g}]_{\infty}$	$1.9106e - 10$	$\text{mol} \cdot \text{cm}^{-3}$	Gaseous CH_4 steady state level	[25]
$[CO_{2,g}]_{\infty}$	$1.19e - 5$	$\text{mol} \cdot \text{cm}^{-3}$	Gaseous CO_2 steady state level	[25]
$[H_{2,g}]_{\infty}$	$3.6505e - 7$	$\text{mol} \cdot \text{cm}^{-3}$	Gaseous H_2 steady state level	[25]
$K_{x,P1}$	20.265	-	Half saturation constant (Comtois law)	[25]
$K_{x,P2}$	0.265	-	Half saturation constant (Comtois law)	[25]
$K_{s,P3}$	$2.6e - 6$	$\text{mol} \cdot \text{cm}^{-3}$	Half saturation for Monod law	[25]
$K_{s,P4}$	$6.626e - 6$	$\text{mol} \cdot \text{cm}^{-3}$	Half saturation for Monod law	[25]
$K_{s,P5}$	$1.7e - 6$	$\text{mol} \cdot \text{cm}^{-3}$	Half saturation for Monod law	[25]
$K_{s,P6}$	$1.563e - 9$	$\text{mol} \cdot \text{cm}^{-3}$	Half saturation for Monod law	[25]
$Y_{m,P1} = Y_{l,P1}$	$8.850e - 3$	-	Yield of component m in process 1,	[25]
$Y_{mon,P1}$	$4.425e - 5$	-	Yield of component mon in process 1,	[25]
$Y_{pol,P2} = Y_{l,P2}$	$8.850e - 3$	-	Yield of component pol in process 2,	[25]
$Y_{mon,P2}$	$4.425e - 5$	-	Yield of component mon in process 2,	[25]
$Y_{mon,P3}$	$8.850e - 3$	-	Yield of component mon in process 3,	[25]
$Y_{B_{mon},P3}$	0.120	-	biomass yield factor for B_{mon} ,	[25]
$Y_{la,P3}$	$4.416e - 3$	-	Yield of component la in process 3,	[25]
$Y_{ac,P3}$	$5.18e - 3$	-	Yield of component ac in process 3,	[25]
$Y_{pro,P3}$	$2.124e - 3$	-	Yield of component pro in process 3,	[25]
$Y_{but,P3}$	$2.389e - 3$	-	Yield of component but in process 3,	[25]
$Y_{CO_2,P3}$	$9.735e - 3$	-	Yield of component CO_2 in process 3,	[25]
$Y_{H_2,P3}$	$1.274e - 2$	-	Yield of component H_2 in process 3,	[25]
$Y_{la,P4}$	$8.850e - 3$	-	Yield of component la in process 4,	[25]
$Y_{B_{la},P4}$	0.120	-	biomass yield factor for B_{la} ,	[25]
$Y_{ac,P4}$	$1.177e - 3$	-	Yield of component ac in process 4,	[25]
$Y_{pro,P4}$	$2.363e - 3$	-	Yield of component pro in process 4,	[25]
$Y_{but,P4}$	$1.770e - 3$	-	Yield of component but in process 4,	[25]
$Y_{CO_2,P4}$	$4.717e - 3$	-	Yield of component CO_2 in process 4,	[25]
$Y_{H_2,P4}$	$3.540e - 3$	-	Yield of component H_2 in process 4,	[25]
$Y_{H_2,P5}$	$8.850e - 3$	-	Yield of component H_2 in process 5,	[25]
$Y_{B_{H_2,a},P5}$	0.043	-	biomass yield factor for $B_{H_2,a}$,	[25]
$Y_{ac,P5}$	$1.265e - 3$	-	Yield of component ac in process 5,	[25]
$Y_{CO_2,P5}$	$-4.424e - 3$	-	Yield of component CO_2 in process 5,	[25]
$Y_{H_2,P6}$	$8.850e - 3$	-	Yield of component H_2 in process 6,	[25]
$Y_{B_{H_2,m},P6}$	0.062	-	biomass yield factor for $B_{H_2,m}$,	[25]
$Y_{CH_4,P6}$	$8.407e - 4$	-	Yield of component CH_4 in process 6,	[25]
$Y_{CO_2,P6}$	$-3.982e - 3$	-	Yield of component CO_2 in process 6,	[25]
$I_{pH,min}$	5.5	-	pH in the proximal part of the gut	[25]
$I_{pH,max}$	6.8	-	pH in the distal part of the gut	[25]
$I_{pH,low}$	5.8	-	Threshold of inhibition	[25]
$I_{pH,high}$	6.7	-	Threshold of inhibition	[25]

Table A.5: Parameter values of the source functions.

Input fluxes on Γ_{in}				
Parameter	Value	Unit	Description	Ref.
U_{in}	$1.5 * 10^3 / (2\pi R^2)$	cm.d^{-1}	Half average surface inflow	[25]
$f_{m,in}$	$f_m(0, r, z)$	[-]	Mucus density input	[25]
$f_{B_{mon},in}$	$6.1e - 5$	[-]	Dietary B_{mon} input	[25]
$f_{B_{la},in}$	$2.03e - 5$	[-]	Dietary B_{la} density input	[25]
$f_{B_{H_2a},in}$	$1.01e - 5$	[-]	Dietary B_{H_2a} density input	[25]
$f_{B_{H_2m},in}$	$1.01e - 5$	[-]	Dietary B_{H_2m} density input	[25]
$f_{pol,in}$	$1.33e - 2$ (i.e. 25g.d^{-1})	[-]	Dietary polysac. density input	[25]
$c_{mon,in}$	$3.33e - 5$	mol.cm^{-3}	Dietary monosac. density input	[25]
Boundary conditions on Γ_m				
f_m^*	0.05	[-]	Mucus threshold at the boundary	[25]
g_m	3	cm.d^{-1}	Mucus production	[25]
$g_{l,max}$	17	cm.d^{-1}	Proximal liquid uptake	-
$g_{l,min}$	2	cm.d^{-1}	Distal liquid uptake	-
L_{pump}^{max}	31.5	cm	Limit of the maximal water uptake	-
L_{pump}^{min}	35.45	cm	Limit of the minimal water uptake	-
$g_{la,max}$	16.85	cm.d^{-1}	Proximal mucosal lactate flow	[25]
$g_{la,min}$	16.29	cm.d^{-1}	Transverse mucosal lactate flow	[25]
$g_{ac,max}$	25.28	cm.d^{-1}	Proximal mucosal acetate flow	[25]
$g_{ac,min}$	24.43	cm.d^{-1}	Transverse mucosal acetate flow	[25]
$g_{bu,max}$	17.23	cm.d^{-1}	Proximal mucosal butyrate flow	[25]
$g_{bu,min}$	16.81	cm.d^{-1}	Transverse mucosal butyrate flow	[25]
$g_{pro,max}$	20.49	cm.d^{-1}	Proximal mucosal propionate flow	[25]
$g_{pro,min}$	19.93	cm.d^{-1}	Transverse mucosal propionate flow	[25]
$U_{per,r}$	0	cm.d^{-1}	Radial peristaltism velocity	??
$U_{per,z}$	-10	cm.d^{-1}	Longitudinal peristaltism velocity	??

Table A.6: **Parameters of the boundary fluxes.**

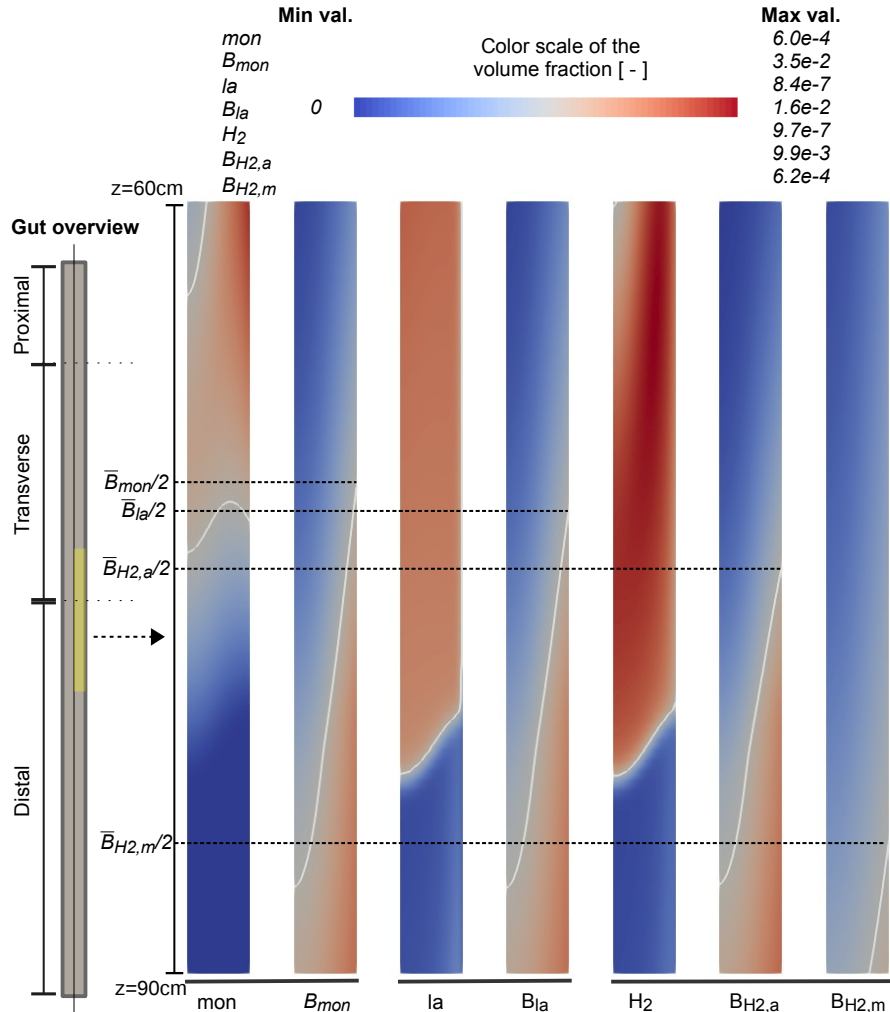


Figure B.1: **Spatial distribution of the trophic chains in the transverse gut.** The steady-state distribution of each bacterial population between $z = 60$ and $z = 90$ cm are displayed together with their respective substrate. We represent also in each plot the isoline of half the maximal value. We indicate with dashed lines the intersection of this isoline with the mucosa, in order to compare the longitudinal position of the bacterial fronts. We note that we represent half a plane of the cylindrical gut; the axis of the cylinder is the left boundary of the images, while the right boundary is the mucosa; the upper part of the images is the most proximal: the digestive flux is then directed from the top to the bottom of the figure. In the gut overview, the domain corresponding to the plots is indicated in yellow. We can observe that the spatial distribution follows the bacterial metabolic functions: the upper is the bacteria in the metabolic graph, the upper in the digestive tract is the bacterial front. The bacteria B_{mon} , metabolizing fibres, is first present, producing substrate for B_{la} . They are both feeding $B_{H_2,a}$ and $B_{H_2,m}$, that are thus located downstream. The population $B_{H_2,m}$, which is repressed by pH, grows more distally.

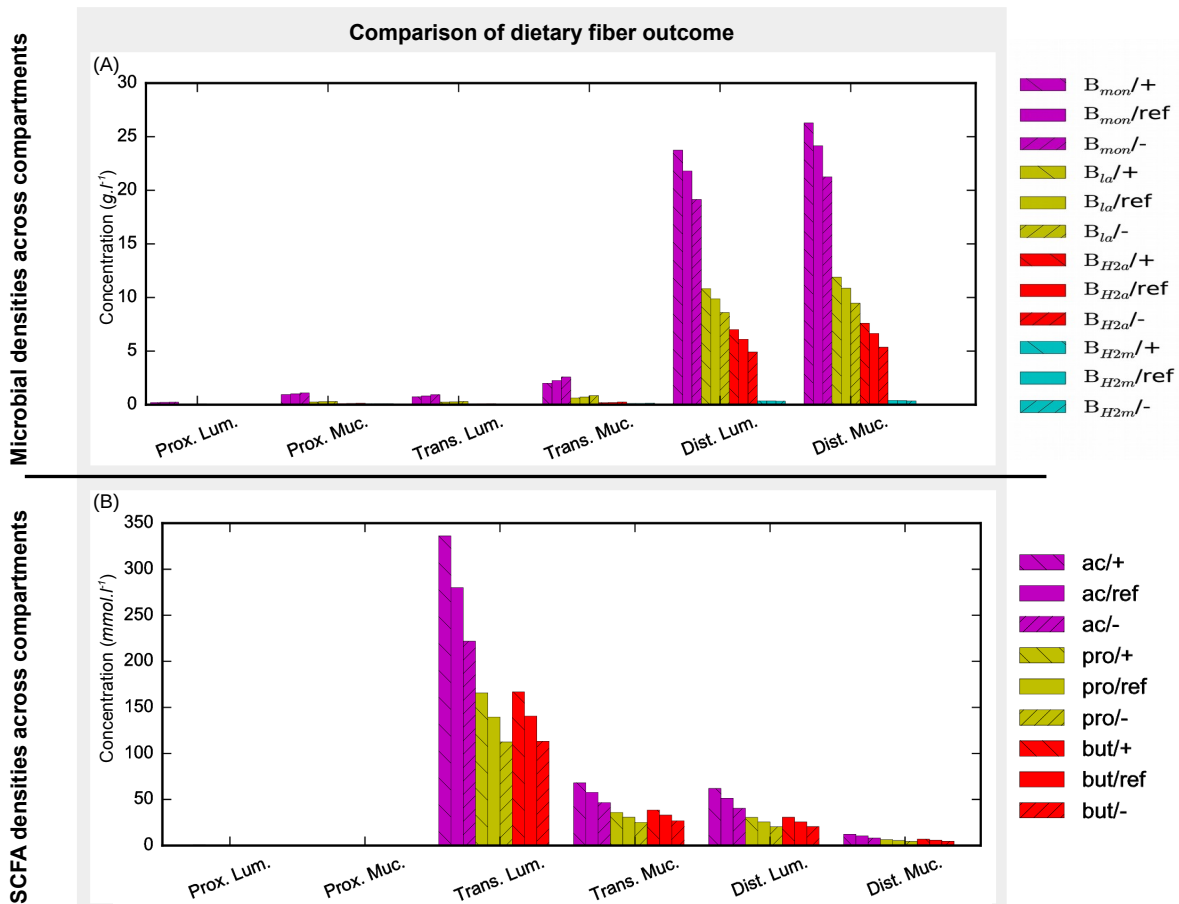


Figure B.2: **Microbial and SCFA levels in the different compartments.** We compare the microbial (A) and SCFA (B) levels during high-fibre(30% increase of polysaccharide input, reverse slash hatches) or low-fibre (30% decrease, slash hatches) diets with reference levels during normal diet (same polysaccharide input, plain boxes). The bacterial and SCFA levels are directly related to the fibre intake.

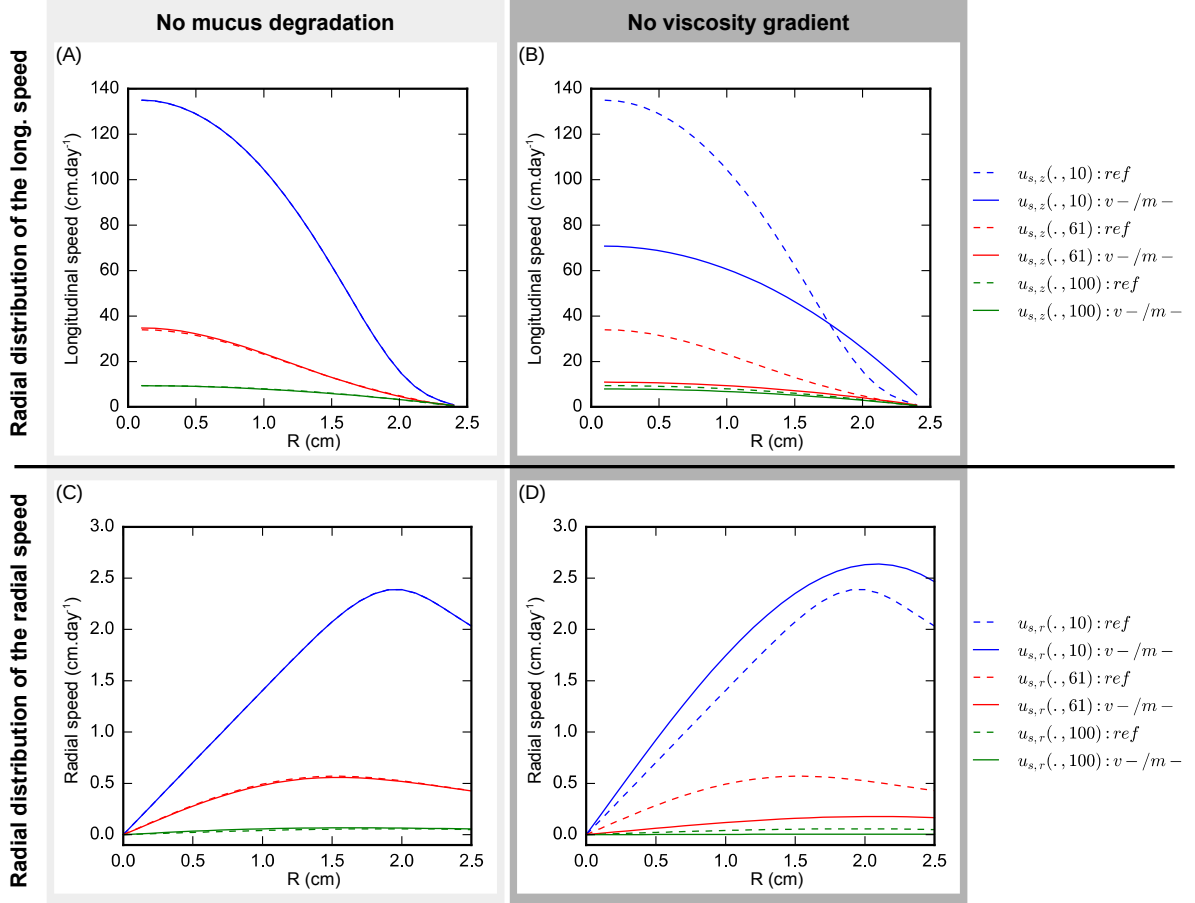


Figure B.3: **Radial distribution of the longitudinal ($u_{s,z}$) and radial ($u_{s,r}$) speeds at $z = 10, 61,$ and 100 cm.** To further explore the drivers of the bacterial activity, we display the radial distribution of the speed components at different lengths with no mucus degradation ($m-$, A and C) or a homogeneous viscosity ($v-$, B and D), compared with the reference of Fig. 2 (*ref*, dashed lines). In the presence of viscosity gradients, we can observe a slower longitudinal speed near the epithelium than with a homogeneous viscosity map (B, dashed and plain blue lines), defining a slow-speed zone near the mucosa. This phenomena is preponderant proximally.

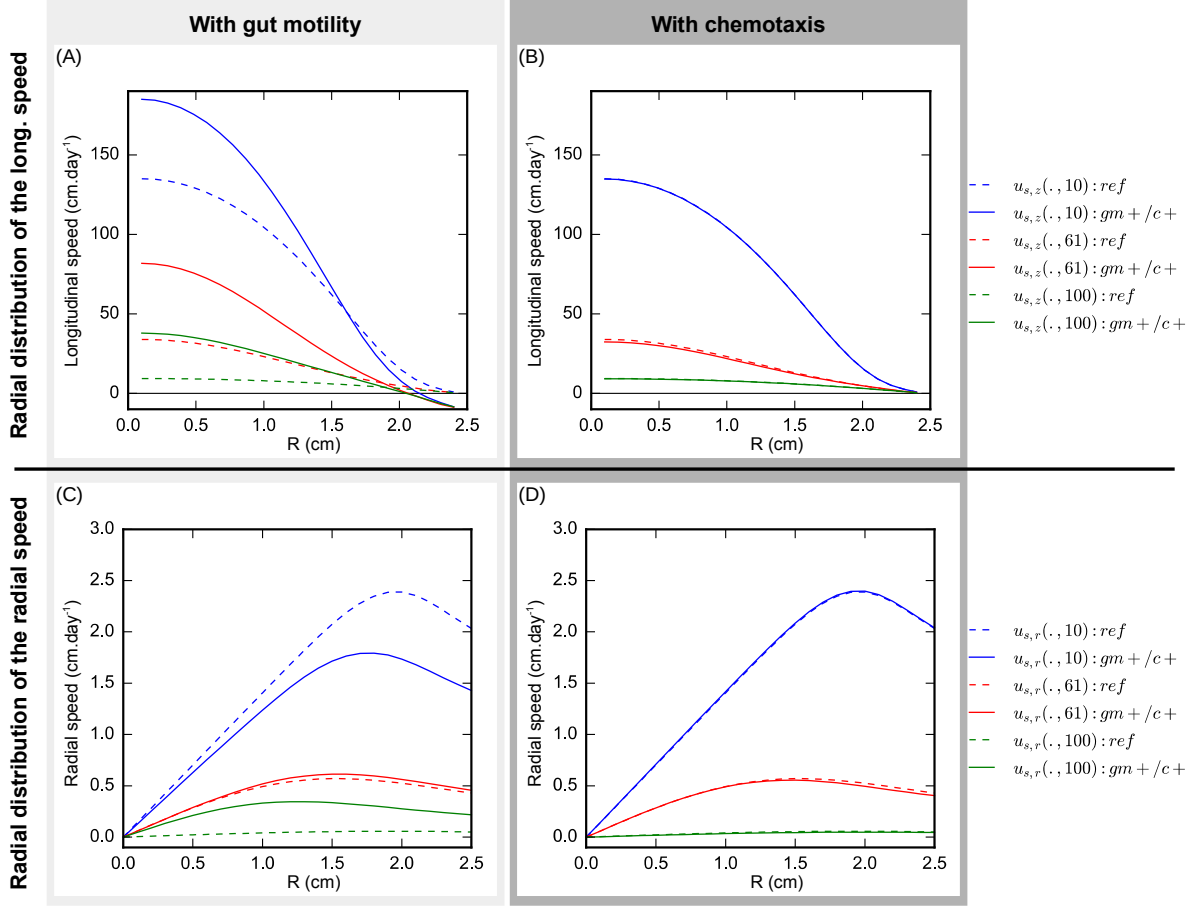


Figure B.4: **Radial distribution of the longitudinal and radial speeds at $z = 10, 61,$ and 100 cm.** To assess the effect of peristalsis and chemotaxis on the spatial structure of intestinal hydrodynamics, we display the radial distribution of the speed components at different lengths with gut motility ($gm+$, A and C) or bacterial chemotaxis ($c+$, B and D), compared with the reference of Fig. 2 (*ref*, dashed lines). When the gut motility is active, negative speeds near the wall are observed, inducing a large increase of the longitudinal speed in the luminal part (blue line, A). Namely, if some material is transported upstream in the wall vicinity, as no outflux is possible in the proximal gut, a higher speed must be applied in the lumen to evacuate this additional material income in order to prevent volume expansion in the proximal gut. The difference of order of magnitudes between the small upstream speed near the mucosa and the large downstream speed at $r = 0$ is due to the cylindrical geometry. In cylindrical coordinates, the elementary volumes near the wall are larger than the luminal ones. Hence, for a same transport speed, the amount of fluid transported in the epithelial vicinity is higher than in the lumen. Consequently, a higher speed must be applied near the gut axis to insure volume conservation.